



# **NAVAL POSTGRADUATE SCHOOL**

**MONTEREY, CALIFORNIA**

## **THESIS**

**AN ANALYSIS OF A DEVELOPING AND  
NON-DEVELOPING DISTURBANCE DURING THE  
PREDICT EXPERIMENT**

by

Thomas M. Freismuth

September 2015

Thesis Advisor:  
Second Reader:

Michael T. Montgomery  
Qing Wang

**Approved for public release; distribution is unlimited**

THIS PAGE INTENTIONALLY LEFT BLANK

<b>REPORT DOCUMENTATION PAGE</b>			Form Approved OMB No. 0704-0188	
Public reporting burden for this collection of information is estimated to average 1 hour per response, including the time for reviewing instruction, searching existing data sources, gathering and maintaining the data needed, and completing and reviewing the collection of information. Send comments regarding this burden estimate or any other aspect of this collection of information, including suggestions for reducing this burden to Washington headquarters Services, Directorate for Information Operations and Reports, 1215 Jefferson Davis Highway, Suite 1204, Arlington, VA 22202-4302, and to the Office of Management and Budget, Paperwork Reduction Project (0704-0188) Washington DC 20503.				
1. AGENCY USE ONLY (Leave Blank)		2. REPORT DATE 09-25-2015		3. REPORT TYPE AND DATES COVERED Master's Thesis 09-30-2013 to 09-25-2015
4. TITLE AND SUBTITLE AN ANALYSIS OF A DEVELOPING AND NON-DEVELOPING DISTURBANCE DURING THE PREDICT EXPERIMENT			5. FUNDING NUMBERS	
6. AUTHOR(S) Thomas M. Freismuth				
7. PERFORMING ORGANIZATION NAME(S) AND ADDRESS(ES) Naval Postgraduate School Monterey, CA 93943			8. PERFORMING ORGANIZATION REPORT NUMBER	
9. SPONSORING / MONITORING AGENCY NAME(S) AND ADDRESS(ES) N/A			10. SPONSORING / MONITORING AGENCY REPORT NUMBER	
11. SUPPLEMENTARY NOTES  The views expressed in this document are those of the author and do not reflect the official policy or position of the Department of Defense or the U.S. Government. IRB Protocol Number: N/A.				
12a. DISTRIBUTION / AVAILABILITY STATEMENT Approved for public release; distribution is unlimited			12b. DISTRIBUTION CODE	
13. ABSTRACT (maximum 200 words)  An analysis is presented of the failed re-development of ex-Gaston and the development of Karl during the 2010 PREDICT field campaign based on the European Centre for Medium Range Weather Forecast (ECMWF) analyses. This study analyzes the flow kinematics and dynamics of ex-Gaston to investigate the role of dry, environmental air in the failed redevelopment. The findings support the hypothesis that entrained, dry air near 600 hPa thwarted convective updraughts and vertical mass flux, which in turn leads to a reduction in vorticity and a compromised pouch at these middle levels. A compromised pouch allows further intrusion of dry air and inhibits vorticity amplification. This study supports recent work investigating the role of dry air in moist convection during tropical cyclogenesis. The circulation and vorticity dynamics of Karl are used to describe the system-scale spin-up within the marsupial paradigm framework. The circulation tendency shows that Karl underwent periods of spin-up and spin-down until its eventual development on 14 September. These spin-up and spin-down episodes correspond with the cycle of convective activity in the Caribbean. The development process is concomitant with recent work describing the genesis and intensification process in developing tropical cyclones.				
14. SUBJECT TERMS tropical cyclogenesis, hurricanes, PREDICT, tropical storms, marsupial paradigm			15. NUMBER OF PAGES 77	
			16. PRICE CODE	
17. SECURITY CLASSIFICATION OF REPORT Unclassified	18. SECURITY CLASSIFICATION OF THIS PAGE Unclassified	19. SECURITY CLASSIFICATION OF ABSTRACT Unclassified	20. LIMITATION OF ABSTRACT UU	

NSN 7540-01-280-5500

Standard Form 298 (Rev. 2-89)  
Prescribed by ANSI Std. Z39-18

THIS PAGE INTENTIONALLY LEFT BLANK



**Approved for public release; distribution is unlimited**

**AN ANALYSIS OF A DEVELOPING AND NON-DEVELOPING DISTURBANCE  
DURING THE PREDICT EXPERIMENT**

Thomas M. Freismuth  
Lieutenant, United States Navy  
B.S., College of Charleston, 2003  
M.S., University of Iowa, 2007

Submitted in partial fulfillment of the  
requirements for the degree of

**MASTER OF SCIENCE IN METEOROLOGY AND PHYSICAL  
OCEANOGRAPHY**

from the

**NAVAL POSTGRADUATE SCHOOL  
September 2015**

Author:	Thomas M. Freismuth
Approved by:	Michael T. Montgomery Thesis Advisor
	Qing Wang Second Reader
	Wendell Nuss Chair, Department of Meteorology

THIS PAGE INTENTIONALLY LEFT BLANK

## **ABSTRACT**

An analysis is presented of the failed re-development of ex-Gaston and the development of Karl during the 2010 PREDICT field campaign based on the European Centre for Medium Range Weather Forecast (ECMWF) analyses. This study analyzes the flow kinematics and dynamics of ex-Gaston to investigate the role of dry, environmental air in the failed redevelopment. The findings support the hypothesis that entrained, dry air near 600 hPa thwarted convective updraughts and vertical mass flux, which in turn leads to a reduction in vorticity and a compromised pouch at these middle levels. A compromised pouch allows further intrusion of dry air and inhibits vorticity amplification. This study supports recent work investigating the role of dry air in moist convection during tropical cyclogenesis.

The circulation and vorticity dynamics of Karl are used to describe the system-scale spin-up within the marsupial paradigm framework. The circulation tendency shows that Karl underwent periods of spin-up and spin-down until its eventual development on 14 September. These spin-up and spin-down episodes correspond with the cycle of convective activity in the Caribbean. The development process is concomitant with recent work describing the genesis and intensification process in developing tropical cyclones.

THIS PAGE INTENTIONALLY LEFT BLANK

---

---

# Table of Contents

---

<b>1</b>	<b>Introduction . . . . .</b>	<b>1</b>
<b>2</b>	<b>Data Sources . . . . .</b>	<b>9</b>
<b>3</b>	<b>Failed Redevelopment of Ex-Gaston . . . . .</b>	<b>13</b>
3.1	Ex-Gaston's Environment . . . . .	13
3.2	Implications of Dry Air and a Degraded Pouch . . . . .	23
<b>4</b>	<b>The Development of Hurricane Karl . . . . .</b>	<b>31</b>
4.1	Pre-Karl's Environment. . . . .	33
4.2	Circulation and Vorticity Dynamics . . . . .	40
4.3	Karl's Spin-Up . . . . .	45
<b>5</b>	<b>Conclusions . . . . .</b>	<b>51</b>
	<b>List of References . . . . .</b>	<b>53</b>
	<b>Initial Distribution List . . . . .</b>	<b>57</b>

THIS PAGE INTENTIONALLY LEFT BLANK

---

## List of Figures

---

Figure 1.1	Schematic depicting the wave-pouch region. The dashed-green lines are the horizontal wind currents of the easterly wave in a Eulerian reference frame. The black curves represent the Lagrangian wave-pouch boundary as revealed in the frame moving with the frame of the easterly wave disturbance. The purple line depicts the critical latitude (CL). The straight black line labeled “Trough” represents the wave-trough axis. The red arrow is an easterly jet. SAL is the dry, Sahara Air Layer. The arrow labeled “Inflow” shows a potential pathway into the wave-pouch (from Montgomery 2010a). . . . .	2
Figure 2.1	Example flights paths for (a) ex-Gaston on 5 September and (b) Karl on 14 September. Flight paths (red lines) are overlaid on minimum pressure contours (blue contours) derived from dropsonde data. Green lines indicate the length and direction of propagation of the sweet spot from the beginning of the research flight to the end of the research flight (from Smith and Montgomery 2012). . . . .	10
Figure 3.1	Track for ex-Gaston based on pouch center (black dots) as identified in the 6 hour, ECMWF analysis data. Green squares show approximate times of PREDICT research flights over the disturbance. The red line indicates when the National Hurricane Center designated the disturbance as at least a tropical depression. The black-dashed line indicated when the disturbance was an incipient wave or remnant low. . . . .	13
Figure 3.2	Average of vertical wind shear magnitude is shown for the 200-850 hPa (red line) and the 500-850 hPa (blue line) levels. Shear decreased from $\sim 20 \text{ m s}^{-1}$ to $\sim 2 \text{ m s}^{-1}$ on 02 September 2010. Although the shear is below the nominal value of $12 \text{ m s}^{-1}$ , there is still persistent shear on the pouch. These results are consistent with previous studies by Davis and Ahijevych (2012). . . . .	15

Figure 3.3	Direction of vertical shear analyzed over a $3^\circ \times 3^\circ$ box centered on the moving sweet spot location. The vertical wind shear is shown for the 200-850 hPa (red line) and the 500-850 hPa (blue line) levels. The directions are compass directions and in a meteorological sense (e.g., $90^\circ$ corresponds to easterly shear). The 500-850 hPa shear is mainly from the north on 02 September 2010. Analysis by RM12 shows that is a source region for dry air. . . . .	16
Figure 3.4	Time-height cross-section of system averaged quantities within a $3^\circ \times 3^\circ$ box from 0000 UTC 30 August to 1800 UTC 06 September. (a) Relative humidity in percent. (b) Relative vorticity ( $\zeta$ ) with relative humidity contours of 40, 50, 60, and 70%. (c) Vertical mass flux with relative humidity contours of 40, 50, 60, and 70%. A dry layer near and above 600 hPa appears on 02 September and persists through 06 September. There are corresponding decreases in relative vorticity and mass flux after 02 September. . . . .	17
Figure 3.5	Dividing streamlines at 1800 UTC 02 September 2010. Dividing streamlines are shown for 500, 700, 850, and 925 hPa, and are overlaid on co-moving wind vectors at each level and total precipitable water. . . . .	18
Figure 3.6	Lagrangian manifolds are overlaid on $\theta_e$ fields at 500 hPa (left column) and 700 hPa (right column) from 01 to 03 September. Stable manifolds are in red, and unstable manifolds are in blue and cyan. The abscissa is longitude and ordinate is latitude. The manifolds indicate that the pouch had a hyperbolic point to the east, but was open to environmental air to the west (figure provided by B. Rutherford, personal communication). . . . .	19
Figure 3.7	Particle trajectory locations at 400 hPa 1800 UTC 31 August are overlaid on $\theta_e$ (K). These trajectories are all within a radius of 3 degrees of the pouch center (green circle) by 1800 UTC, 02 September. The abscissa is longitude and ordinate is latitude (figure provided by B. Rutherford, personal communication). . . . .	20
Figure 3.8	Particle trajectory locations at 500 hPa 1800 UTC 31 August are overlaid on $\theta_e$ (K). These trajectories are all within a radius of 3 degrees of the pouch center (green circle) by 1800 UTC 02 September. The abscissa is longitude and ordinate is latitude (figure provided by B. Rutherford, personal communication). . . . .	21



Figure 3.9	$\theta_e$ vs. radial distance from the center of ex-Gaston's pouch. The colors range from brown to blue, with brown denoting the earliest time of 0000 UTC 31 August and blue denoting the latest time of 1800 UTC 02 September (figure provided by B. Rutherford, personal communication). . . . .	22
Figure 3.10	Height-time series of maximum vertical velocities from the numerical experiments of KS12 using the (a) moist profile and the (b) dry profile from PREDICT. Red lines are positive (updraught) and blue-dashed lines are negative (downdraughts). Thin contours are $2 \text{ m s}^{-1}$ and thick contours are $4 \text{ m s}^{-1}$ . Thick black contours indicate values above $20 \text{ m s}^{-1}$ in $5 \text{ m s}^{-1}$ intervals (from KS12). . . . .	24
Figure 3.11	Comparison for moist (a) and dry (c) soundings from 05 September used by KS12 with typical moist (b) and dry (d) soundings from 02 September. Solid lines indicate temperature and dashed-lines indicate dew point temperature. Flight paths (white) for 05 September (e) and 02 September (f) are overlaid on the RH field at 700 hPa (shading) and co-moving streamlines (black lines). Blue and red dots indicate the locations of the selected moist and dry soundings, respectively, for each day. . . . .	26
Figure 3.12	PREDICT flight path and dropsonde locations (white line with white points) overlaid on 700 hPa relative humidity (shading) and co-moving streamlines from ECMWF analysis data at 1800 UTC 02 September. The gray Xs indicate locations where dropsonde data show evidence of an inversion. The black box corresponds to GR14 Figure 8. The expanded box shows the skew T - ln P diagrams from the 02 September PREDICT flight dropsondes within the GR14 area of interest. Only the profile in the northwest corner in the black box shows evidence of an inversion. . . . .	29
Figure 3.13	Particle trajectory locations at 850 hPa at 0000 UTC 04 September overlaid on $\theta_e$ (K). Particles were seeded west of ex-Gaston's pouch at 1200 UTC 02 September, within a suspected trade wind inversion layer. These trajectories are all outside of a 3 degree radius of the pouch center (green circle) on 04 September. The abscissa is longitude and ordinate is latitude (figure provided by B. Rutherford, personal communication). . . . .	30

Figure 4.1	Track for Karl based on pouch center (black dots) as identified in the 6 hour, ECMWF analysis data. Green squares show approximate times of PREDICT research flights over the disturbance. The red line indicates when the National Hurricane Center designated the disturbance as at least a tropical depression. The black-dashed line indicated when the disturbance was an incipient wave or remnant low. . . . .	31
Figure 4.2	85 GHz montage for Karl's track from 10 to 17 September. Warmer colors indicate active convection (from Montgomery et al. 2012).	32
Figure 4.3	Time-radius diagram of cloud-top temperatures derived from GOES IR data. Temperatures are the 75th percentile temperature within each radial ring of 20 km. The dashed line indicates the time of genesis. The black arrows indicate the times of GV PREDICT flights and the red arrows indicate times of research flights by NOAA or NASA (from Davis and Ahijevych 2012). . . . .	33
Figure 4.4	Average of vertical wind shear magnitude is shown for the 200-850 hPa (red line) and the 500-850 hPa (blue line) levels. . . . .	34
Figure 4.5	Direction of vertical shear analyzed over a $3^\circ \times 3^\circ$ box centered on the moving sweet spot location. The vertical wind shear is shown for the 200-850 hPa (red line) and the 500-850 hPa (blue line) levels. The directions are compass directions in a meteorological sense (e.g., $90^\circ$ corresponds to easterly shear). . . . .	35
Figure 4.6	Time-height cross-section of system averaged quantities within a $3^\circ \times 3^\circ$ box from 0000 UTC 09 September to 0000 UTC 17 September. (a) Relative humidity in percent. (b) Relative vorticity ( $\zeta$ ) with relative humidity contours of 40, 50, 60, and 70%. (c) Vertical mass flux with relative humidity contours of 40, 50, 60, and 70%. . . . .	36
Figure 4.7	Time-height plot of $\theta_e$ averaged over a $3^\circ \times 3^\circ$ box from 09 to 17 September. Higher values of $\theta_e$ indicate greater moisture. . . . .	37
Figure 4.8	Evolution of $\zeta$ averaged over $3^\circ \times 3^\circ$ box at the 500, 700, 850, and 950 hPa pressure levels. The time is from 0000 UTC 09 September to 0000 UTC 17 September. Genesis occurred at approximately 1800 UTC 14 September. . . . .	38

Figure 4.9	Time-radius plots of average $\zeta$ . $\zeta$ was averaged over a $1^\circ \times 1^\circ$ box centered on the 700 hPa (tracking level) sweet spot, and subsequently averaged within $0.5^\circ$ wide concentric square annuli. Results are shown for the 700 hPa (a) and 950 hPa (b) levels. . . . .	39
Figure 4.10	Depiction of vorticity fluxes (from Raymond et al. 2014). . . . .	41
Figure 4.11	Time-height cross-sections of circulation (top), absolute vorticity convergence (middle), and vortex tilting (bottom) tendencies (shading) from 1800 UTC 11 September to 0000 UTC 12 September. The dashed line represents the zero contour level on each panel. This time interval is chosen to illustrate a low-level spin-down phase as indicated in Figures 4.6 and 4.8. . . . .	42
Figure 4.12	Time-height cross-sections of circulation (top), absolute vorticity convergence (middle), and vortex tilting (bottom) tendencies (shading) from 0000 UTC to 0600 UTC 12 September. The dashed line represents the zero contour level on each panel. This time interval is chosen to illustrate a low-level spin-up phase as indicated in Figures 4.6 and 4.8. . . . .	43
Figure 4.13	Time-height cross-sections of circulation (top), absolute vorticity convergence (middle), and vortex tilting (bottom) tendencies (shading) from 1200 UTC to 1800 UTC 14 September. The dashed line represents the zero contour level on each panel. NHC designated Karl a tropical storm at 2100 UTC 14 September. . . . .	44
Figure 4.14	Absolute angular momentum surfaces (red and pink contours) at (a) initial time, and (b) 48 hours later from an idealized numerical experiment. The cyan contour indicates an $M$ value of $20 \times 10^5 \text{ m}^2 \text{ s}^{-1}$ , and the yellow region indicates values greater than $32 \times 10^5 \text{ m}^2 \text{ s}^{-1}$ . Black contours in (b) are tangential velocity, and blue contours in (c) are radial velocities at 48 hours. The black contour in (c) delineates regions where conditions are met for axisymmetric instability (Montgomery and Smith 2014). (d) Depiction of the spin-up process (from Montgomery and Smith 2014). . . . .	47
Figure 4.15	Pre-Karl circulation centers at 500 hPa (blue) and 900 hPa (red). The date and time of the analysis is indicated by the blue labels. The size of the circle is related to the spatial extent of the circulation (from Davis and Ahijevych 2012). . . . .	48

Figure 4.16 Evolution of average tangential velocity (shading) and angular momentum surfaces (contours) from 1800 UTC 11 September to 1800 UTC 16 September in 24 hour intervals as examples. The ordinate is pressure from 200 to 950 hPa and the abscissa is the size of a box centered on the sweet spot. Contours are shown for  $0.5 \times 10^6 \text{ m}^2 \text{ s}^{-1}$  intervals with the 1, 3, 5, and  $7 \times 10^6 \text{ m}^2$  contours highlighted in white. . . . . 49

---

---

## List of Tables

---

Table 3.1	Summary of Dropsondes from PREDICT Research Flight 9 (RF09) on 02 September (after Smith and Montgomery 2012). . . . .	28
-----------	---	----

THIS PAGE INTENTIONALLY LEFT BLANK

---

---

## Acknowledgments

---

I am forever grateful for my family and their ever-enduring patience and support during the course of this research. I would like to thank my advisor, Professor Montgomery, for his enthusiastic approach to science and sharing his passion for geophysical fluid dynamics and tropical meteorology. This work would not have been possible without the critical support from Mark Boothe and Blake Rutherford. Thank you to Professor Wang and Professor Nuss for their careful reading of this thesis and valuable input. Additionally, I would like to thank my section leader, LCDR Darin Keeter, for his mentorship and friendship.

THIS PAGE INTENTIONALLY LEFT BLANK



---

# CHAPTER 1:

## Introduction

---

A major, unsolved problem in dynamical meteorology has been the genesis of tropical cyclones, hurricanes, and typhoons. A fundamental problem in understanding tropical cyclogenesis is describing the interaction of the approximately conserved properties of potential vorticity and moist entropy. In the innovative work of Dunkerton et al. (2009), hereafter DMW09, the authors propose a new framework for understanding these interactions in tropical cyclogenesis. In their description of tropical cyclogenesis, DMW09 use a Lagrangian viewpoint to describe the interaction of an easterly tropical wave, the synoptic environment, and deep convection. As the wave propagates primarily westwards, the flow establishes dynamic flow boundaries (a Kelvin cat's eye) that effectively trap moist parcels. The region where this trapping occurs is referred to as the "wave-pouch." This pouch is centered about the intersection of the wave trough-axis and the critical latitude (Figure 1.1). The critical latitude is the latitude where the mean flow and wave phase speeds are equal (DMW09).

This new framework is referred to as the marsupial paradigm. The analogy being that a marsupial protects its young in a pouch, safe from a hostile environment. As an easterly wave propagates westward, it can provide a region where an incipient proto-vortex is protected from hostile environmental conditions, such as vertical shear or dry air. The tropical wave supports the growth of the proto-vortex until it has intensified and is self-sustaining. In a study by Wang et al. (2009), the authors found that there was a "sweet spot" (Figure 1.1) or preferred location for genesis. The sweet spot is the intersection of the critical latitude and the wave trough-axis described by DMW09.

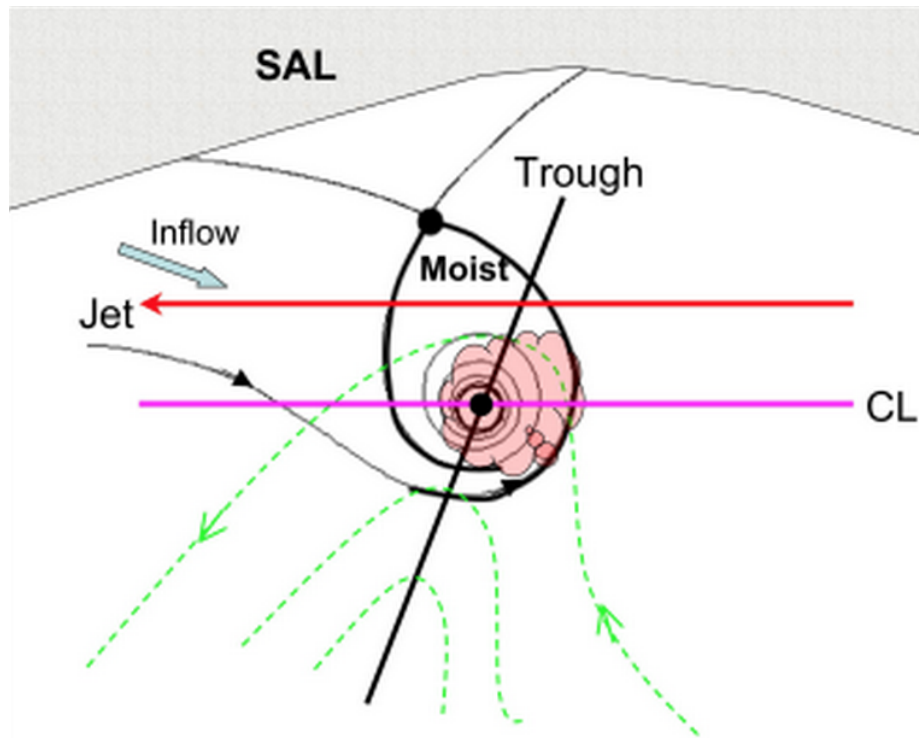


Figure 1.1: Schematic depicting the wave-pouch region. The dashed-green lines are the horizontal wind currents of the easterly wave in a Eulerian reference frame. The black curves represent the Lagrangian wave-pouch boundary as revealed in the frame moving with the frame of the easterly wave disturbance. The purple line depicts the critical latitude (CL). The straight black line labeled “Trough” represents the wave-trough axis. The red arrow is an easterly jet. SAL is the dry, Sahara Air Layer. The arrow labeled “Inflow” shows a potential pathway into the wave-pouch (from Montgomery 2010a).

Framed by this marsupial paradigm, DMW09 pose three, testable hypotheses for tropical cyclogenesis:

1. The cat’s eye region within the critical layer has cyclonic recirculation with little strain deformation, and its center serves as the focal point for vorticity aggregation of convectively generated cyclonic vertical vorticity and their vortical remnants.
2. Air inside the cat’s eye is repeatedly moistened by convection and is protected to some extent from the lateral intrusion of dry air.
3. The parent wave is maintained and possibly enhanced by convectively am-

plified mesoscale eddies within the wave. (Rutherford and Montgomery 2012)

The new cyclogenesis model and accompanying scientific hypotheses were established observationally in the Atlantic and eastern Pacific sectors by DMW09.

In order to get a better understanding of tropical cyclogenesis and test the marsupial paradigm, the Pre-Depression Investigation of Cloud Systems in the Tropics (PREDICT) experiment was conducted during the 2010 Atlantic hurricane season (Montgomery et al. 2012). This experiment was designed to identify tropical waves before they were identified as tropical depressions. The environmental characteristics of these mesoscale systems were measured primarily by dropsonde delivered by a Gulfstream V (GV). The aircraft was operated from St. Croix, U.S. Virgin Islands, and had an operational range from the Atlantic Basin to Central America at a range of cruising altitudes between 12 km to 14 km.

PREDICT Mission scientists used “pouch tracking” techniques (Boothe 2015a) based on the marsupial paradigm to identify potential systems. Pouch tracking involves using model forecasts to analyze the evolution of tropical disturbances from a Lagrangian perspective, as well as environmental properties like vertical shear and relative humidity. This method allows forecasters to predict the likelihood of the development tropical disturbances. The PREDICT experiment investigated eight tropical systems; two nondeveloping African waves, three developing waves, one developing Caribbean gyre, one failed redevelopment of an African wave, and one system of undetermined fate (Montgomery et al. 2012, Table 2 therein). There were a total of 25 research flights over 24 days with 561 dropsondes deployed. The PREDICT experiment provided an unprecedented amount of in-situ observations of developing and nondeveloping tropical systems. Concurrent with the PREDICT experiment, NASA and the National Oceanic and Atmospheric Administration (NOAA) were also conducting experiments to study the tropical disturbances. The NASA Genesis and Rapid Intensification Processes (GRIP) used a DC-8 aircraft to deploy dropsondes in tropical disturbances. The NOAA Intensity Forecasting Experiment (IFEX) was primarily focused on observing developed systems, and used a G-IV to deploy dropsondes and two WP-3 aircraft to deploy dropsondes and perform airborne Doppler radar observations.

One of the first studies of PREDICT data was performed by Smith and Montgomery (2012). In their study, the authors characterized the convective environments of three sys-

tems. Two of the systems underwent genesis: pre-Karl developed into Hurricane Karl and pre-Matthew developed into tropical storm Matthew. The other system, named Gaston, achieved tropical storm status briefly, but eventually weakened and failed to redevelop. Because this system never redeveloped into a tropical storm, it is referred to hereafter as ex-Gaston. Smith and Montgomery (2012) calculated the convective available potential energy (CAPE), convective inhibition (CIN), and moisture properties. They found that the lower troposphere tended to become progressively more moist, but in the case of ex-Gaston the troposphere became drier between an altitude of 2 and 9 km. Based on these findings, Smith and Montgomery (2012) hypothesized that dry air (or “anti-fuel”) weakened the convective updraughts of ex-Gaston and limited the amplification of absolute vorticity, thereby preventing the system from redeveloping. Sauer (2014) performed a complimentary study where he analyzed the dropsonde data for the PREDICT systems not reported in Smith and Montgomery (2012). Komaromi (2013) analyzed composite dropsonde data for the developing and non-developing system during PREDICT and had similar findings as Smith and Montgomery (2012), namely progressive moistening during the developing cases and progressive drying during the non-developing cases.

Wang (2012) provided additional evidence for a progressive moistening of the pouch in developing cases, and drying in non-developing cases. Wang (2012) used numerical simulations of the development of Hurricane Felix (2007), studied earlier by Wang et al. (2010a,b), using the Weather Research and Forecasting (WRF) Model and PREDICT data to examine thermodynamic variables as a function of radius from the disturbance’s sweet-spot. She found that for developing tropical cyclones, the inner pouch region is moist compared to the outer pouch region, and becomes progressively more moist as the system organizes. Based on the results of Wang (2012), it seems reasonable to attribute the favorable thermodynamic conditions to the minimal shear and strain within a protective pouch.

Davis and Ahijevych (2012) used the PREDICT data to study the structural evolution of ex-Gaston, Karl, and Matthew (the same systems analyzed by Smith and Montgomery 2012). They found that ex-Gaston started as a moist core surrounded by a dry environment, and vertical shear caused the circulation centers to be vertically misaligned. Davis and Ahijevych (2012) conclude that the dry air limited the convective activity by enhancing the

potential for downdraughts near ex-Gaston's pouch. They also found that Karl's circulation centers were initially vertically misaligned, but aligned later during its evolution. After the alignment, Karl underwent genesis within a moist environment. Matthew also formed within a moist environment, and was vertically aligned throughout its relatively rapid development. Davis and Ahijevych (2012) concluded that the marsupial paradigm helps to explain a level of predictability of tropical cyclogenesis.

In a study by Rutherford and Montgomery (2012), the authors introduced a new method for analyzing tropical cyclogenesis. They examined the flow topology and flow boundaries in ex-Gaston and Karl using the ECMWF model data. The Lagrangian methods presented by Rutherford and Montgomery (2012) test the first and second hypotheses of the marsupial paradigm. First, the authors were able to calculate the flow boundaries and identify a pouch. Second, Rutherford and Montgomery (2012) used particle trajectories to identify possible dry air intrusion. Third, they showed evolution of relative vorticity within the pouch for ex-Gaston and Karl. Rutherford and Montgomery (2012) showed that ex-Gaston had a pouch that was open to hostile, dry air which they argued led to this system's failed redevelopment. Further, they found similar results as Davis and Ahijevych (2012), namely Karl initially had a vertically misaligned pouch, that eventually aligned, and the system underwent genesis.

The marsupial paradigm finds additional support in idealized numerical modeling simulations (Montgomery et al. 2010b; Nicholls and Montgomery 2013; Wang et al. 2010a,b), recent case studies in the field in the western North Pacific during the Tropical Cyclone Structure Experiment 2008 (TCS08, Lussier III 2010; Lussier III et al. 2014; Montgomery et al. 2010a, 2012; Raymond and Lopez-Carrillo 2011), in NASA's ongoing Hurricane and Severe Storm (HS3) missions (2012-15), and the case of Hurricane Sandy (Lussier III et al. 2015). The field data afford a resolved view of horizontal and vertical structure in the wave pouch and its immediate surroundings, valuable for system centering, circulation magnitude, vorticity balance, interleaving of air masses, and moist thermodynamic profiles.

A somewhat different perspective on tropical cyclogenesis is offered by Raymond and Sessions (2007) and Raymond and Lopez-Carrillo (2011). In a review of the numerical experiments of Raymond and Sessions (2007), Raymond and Lopez-Carrillo (2011, p. 147) summarized their findings as follows: "Environments cooler at low levels and warmer at

upper levels of order 1 K lower the elevation of maximum vertical mass flux from  $\approx 10$  km to  $\approx 5$  km in their calculations, and by virtue of mass continuity, intensify the low-level inflow into the convection. In the presence of ambient vorticity, low-level convergence would contribute to the spinup of the system." In this paradigm for tropical cyclogenesis, the vorticity dynamics are slaved to the thermodynamics and mass continuity.

This thesis focuses on the non-developing case of ex-Gaston (2010) and the developing case of Karl (2010) in the European Centre for Medium-Range Weather Forecasts (ECMWF) model. As discussed above, both of these systems were observed during the PREDICT experiment. Ex-Gaston is arguably one of the most extensively observed non-developing tropical disturbances ever. During the PREDICT mission, there were five GV research flights over five days with a total of 109 dropsondes conducted and later ingested into the ECMWF model.

Gjorgjievska and Raymond (2014, hereafter referred to as GR14) have proposed a different process for the failed redevelopment of ex-Gaston (discussed in detail Chapter 3.2). GR14 question the structure of ex-Gaston's pouch, as well as the role and efficacy of dry air in frustrating ex-Gaston's redevelopment. This thesis answers two fundamental questions: (1) Did ex-Gaston have a robust pouch? (2) What was the role of dry-air, or anti-fuel, in ex-Gaston's failed redevelopment?

Unlike ex-Gaston, Karl underwent genesis and developed into a major hurricane. The PREDICT experiment began investigating this system nearly four days prior to genesis. This represents one of the earliest (with respect to time of genesis) and most observed developing systems. For Karl, there were six PREDICT research flights over five days with 127 dropsondes conducted and later ingested into the EMCWF model. This thesis aims to establish the spin-up process for Karl.

In closing this Introduction, it is useful to recall that a better understanding of the physics of tropical cyclogenesis would seem to be a necessary element for improving the prediction of storm development. An understanding of tropical cyclogenesis is of vital importance to the United States Navy. As humanitarian assistance and disaster relief becomes an increasingly important mission to promote regional stability, the navy will need to be effective at anticipating the vast destruction caused by tropical cyclones. A thorough understanding of

genesis will allow vital navy assets (e.g., carrier strike groups, amphibious ready groups, or the USNS Mercy or USNS Comfort) to anticipate when and where a tropical cyclone will form. This could provide a nearly 48-hour lead time for pre-positioning. In order to maximize an efficient response while still protecting the fleet, decision makers rely on accurate and timely, environmental information. Navy Meteorology and Oceanography, therefore, needs the most current and innovative approaches for effective tasking, collection, processing, exploitation, and dissemination of tropical cyclone decision aids and recommendations to the fleet.

THIS PAGE INTENTIONALLY LEFT BLANK



---

## CHAPTER 2:

### Data Sources

---

This study uses the European Centre for Medium-Range Weather Forecasts (ECMWF) analysis fields. The ECMWF model is a two-time-level, semi-implicit, semi-Lagrangian spectral model that solves the Euler equations of motions using the hydrostatic approximation. The horizontal discretization uses a reduced Gaussian grid, while the vertical model is discretized using a finite-element scheme. The ECMWF model is able to resolve flow features to  $\sim 1^\circ$ . The ECMWF model uses a four-dimensional variational analysis (4DVAR) system to incorporate observations into the model forecast. As summarized in the Introduction and in Montgomery et al. (2012), the PREDICT data consisting of the NSF GV dropsondes, together with the NASA DC-8 and NOAA G-IV and P3 dropsondes, were incorporated into the ECMWF model. The resulting model analyses have a horizontal grid size of  $0.25^\circ$ , 25 vertical levels from 1 to 1000 hPa, and temporal output every 6-hours.

Subgrid-scale process (e.g., radiation, clouds, and turbulent diffusion) are modeled through physical parameterization schemes of the model. ECMWF uses a moist convection scheme based on Tiedtke mass-flux approach (described in Tiedtke 1989) with a modified CAPE closure and an improved entrainment formulation. Bechtold et al. (2008) and Bechtold et al. (2014) describe the convection parameterization for ECMWF in detail. The radiation scheme uses the Rapid Radiation Transfer Model (Mlawer et al. 1997; Morcrette et al. 2008) to compute the subgrid-scale radiative fluxes based on the predicted state of the atmosphere. ECMWF uses two different turbulent diffusions schemes: (1) a first order K-diffusion closure based on Monin-Obukhov similarity theory in the surface layer, and (2) above the surface layer an Eddy-Diffusivity Mass-Flux scheme is used for unstable boundary layers (Köhler et al. 2011).

PREDICT mission scientists used model forecasts to design flight plans to investigate tropical disturbances during the experiment. The proposed flight plans attempted to perform dropsondes in a uniform grid with  $\sim 1^\circ$  horizontal separation between drops (Figure 2.1). Because of flight restrictions from weather or international boundaries, some flight plans were altered and attaining a uniform distribution of dropsondes through the disturbance

was not possible (Montgomery et al. 2012). In the NSF supported PREDICT project, there were 5 research flights with 109 dropsondes conducted during ex-Gaston, and 6 research flights with 127 dropsondes conducted during Karl. Coincident with PREDICT, both the GRIP and IFEX experiments were also underway. The GRIP experiment used a NASA DC-8 aircraft to perform dropsondes into tropical disturbances. The IFEX experiment used G-IV and WP-3 aircrafts, and performed dropsondes in Karl and Matthew. The GRIP and IFEX data augmented the PREDICT dropsonde data set. The ECMWF model analyses used herein incorporate the PREDICT, the GRIP, and IFEX dropsonde data.

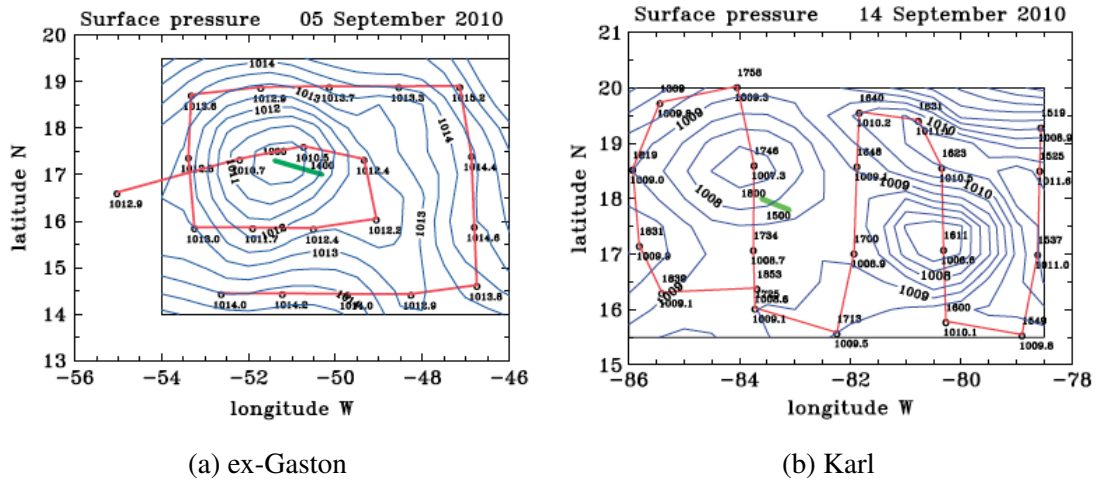


Figure 2.1: Example flights paths for (a) ex-Gaston on 5 September and (b) Karl on 14 September. Flight paths (red lines) are overlaid on minimum pressure contours (blue contours) derived from dropsonde data. Green lines indicate the length and direction of propagation of the sweet spot from the beginning of the research flight to the end of the research flight (from Smith and Montgomery 2012).

For this thesis, the ECMWF analyses from 28 August to 11 September are used for ex-Gaston, and the analyses from 09 to 17 September are used for Karl. The sweet spot is determined through the following process: First, the wave-trough axis is determined in the ECMWF analyses as any line in an area of positive relative vorticity above  $1 \times 10^{-6} \text{ s}^{-1}$  along which meridional wind is zero. Second, the phase speed of the wave is resolved by determining the propagation of the meridional wind, total precipitable water, and/or relative humidity with Hovmoeller diagrams. Third, the sweet spot is then identified as the intersection of the wave-trough axis with the surface where zonal wind is equal to the phase

speed of the wave (critical latitude).

THIS PAGE INTENTIONALLY LEFT BLANK

---

## CHAPTER 3:

### Failed Redevelopment of Ex-Gaston

---

Tropical Storm Gaston developed from an African easterly wave that moved westward from the African coast on 28 August 2010. The National Hurricane Center designated Gaston as a tropical storm at 1500 UTC 01 September. Despite being in a favorable environment with low shear and a SST of 28.5°C (Gjorgjievska and Raymond 2014), convection associated with Gaston quickly diminished, and NHC downgraded Gaston to a remnant low by 1800 UTC 02 September. Convective activity increased on 03 September, however it did not re-organize and the system remained a remnant low (Figure 3.1).

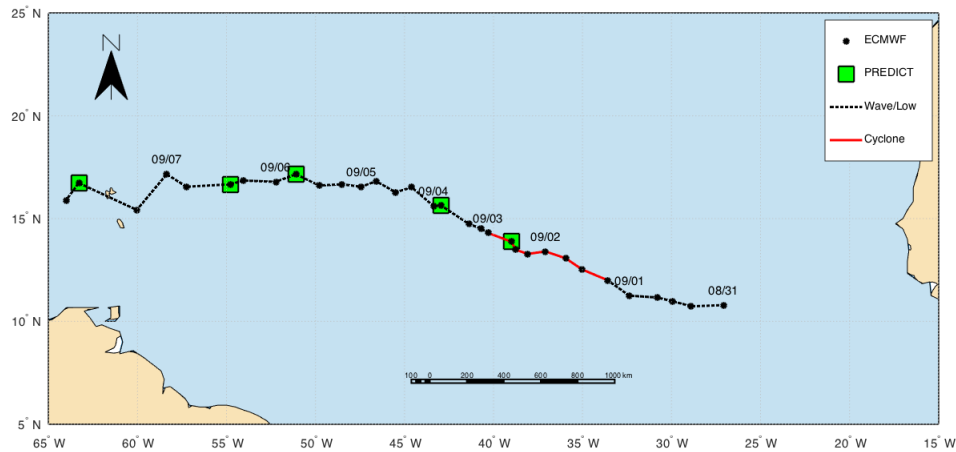


Figure 3.1: Track for ex-Gaston based on pouch center (black dots) as identified in the 6 hour, ECMWF analysis data. Green squares show approximate times of PREDICT research flights over the disturbance. The red line indicates when the National Hurricane Center designated the disturbance as at least a tropical depression. The black-dashed line indicated when the disturbance was an incipient wave or remnant low.

### 3.1 Ex-Gaston's Environment

This analysis begins by characterizing the vertical shear that affected Gaston's pouch. "Deep-layer shear" and "pouch shear" are computed by taking the vector differential of

horizontal winds between the 200 hPa and 850 hPa levels, and between the 500 hPa and 850 hPa levels, respectively, averaged over a  $3^\circ \times 3^\circ$  box centered at the pouch center. The pouch-scale averaging is performed on a  $3^\circ \times 3^\circ$  box, centered on the circulation center as defined by the 700 hPa tracking level.

For both the deep and pouch shear, the magnitude of the shear decreases rapidly from  $\sim 20 \text{ m s}^{-1}$  on 30 August to  $\sim 2 \text{ m s}^{-1}$  on 02 September (Figure 3.2). During the same period, the direction of the deep and pouch shear shifts from easterly to westerly flow (Figure 3.3). After 02 September, the magnitude of the shear (deep and pouch) increases to  $\sim 5 \text{ m s}^{-1}$ . The pouch shear direction slowly becomes more northerly by 05 September. The deep shear, though, rapidly changes direction from northeasterly to southwesterly from 1200 UTC 02 September to 0000 UTC 03 September, in the ECMWF data. The deep shear returns to an easterly flow on 04 September. These shear results are consistent with the analysis of PREDICT data by Davis and Ahijevych (2012). The National Hurricane Center defines vertical shear of  $12 \text{ m s}^{-1}$  as an upper limit for favorable conditions for tropical cyclogenesis. The magnitude of the vertical shear (typically  $4\text{--}8 \text{ m s}^{-1}$ ) for ex-Gaston, while below this heuristic limit for a SST of  $28.5^\circ\text{C}$ , does suggest lateral flow and a potential contribution of dipole-like distribution of vorticity from a non-advective flux (Haynes and McIntyre 1987; Raymond et al. 2014). This contribution could be a net increase or decrease of vorticity.

The evolution of other pertinent variables is shown in Figure 3.4. In the subpanels of this figure, shown are time-height Hovmoeller diagrams of relative humidity, relative vorticity ( $\zeta$ ), and vertical mass flux at each level from averages taken over a  $3^\circ \times 3^\circ$  box (referred to as pouch scales). A similar analysis was done for a  $1^\circ \times 1^\circ$  box (referred to as sub-pouch scale) centered on the circulation center; trends were similar to those for the 3 degree box, but are not shown. This analysis uses the model vertical velocity in pressure coordinates,  $\omega$ , to calculate the mass flux as  $\rho w = -\omega/g$ , where  $\rho$  is density,  $w$  is vertical velocity in height coordinates, and  $g$  is the acceleration due to gravity. On both the pouch and sub-pouch scales in the ECMWF data, a layer of dry air above 600 hPa appears to penetrate the pouch region on 02 September, and that dry layer persists through the decline of the system (Figure 3.4). Coincident with the intrusion of the dry air are decreases in the system-scale relative vorticity and mass flux.

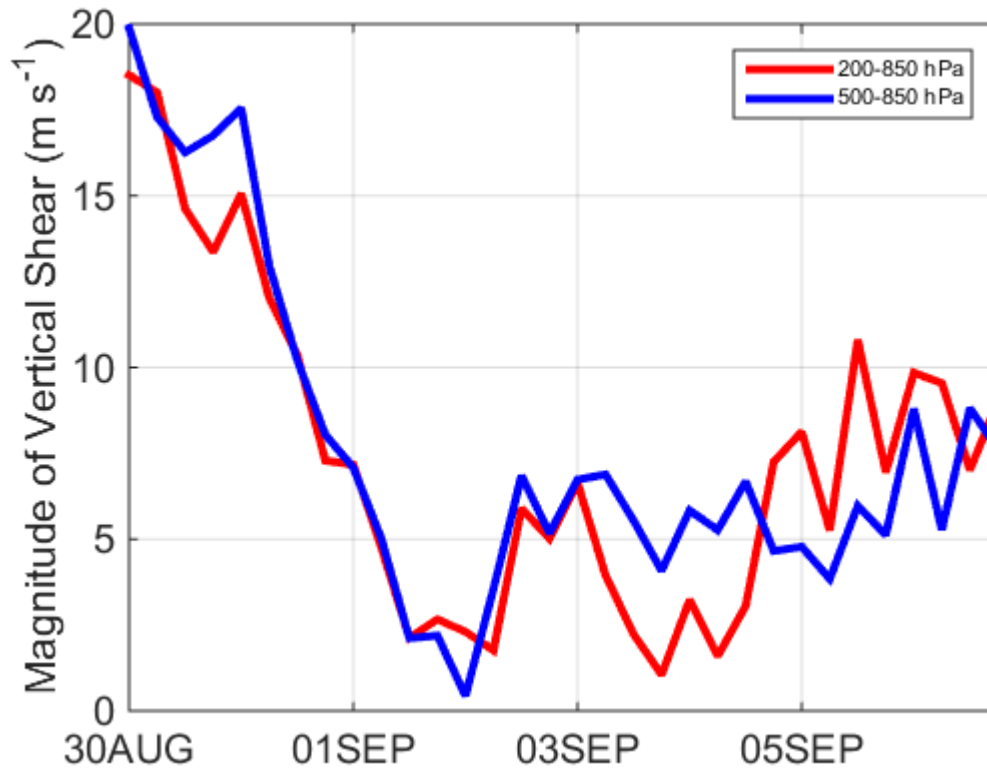


Figure 3.2: Average of vertical wind shear magnitude is shown for the 200-850 hPa (red line) and the 500-850 hPa (blue line) levels. Shear decreased from  $\sim 20 \text{ m s}^{-1}$  to  $\sim 2 \text{ m s}^{-1}$  on 02 September 2010. Although the shear is below the nominal value of  $12 \text{ m s}^{-1}$ , there is still persistent shear on the pouch. These results are consistent with previous studies by Davis and Ahijevych (2012).

To gain insight into the apparent intrusion of dry air into the pouch beginning near 0600 UTC 02 September (discussed above), this study first examines the flow topology of ex-Gaston using the dividing streamline methodology discussed in Riemer and Montgomery (2011). This methodology assumes for simplicity that the flow is steady in a translating frame. Although the observed flow will be shown later to have an important transient component, this technique can provide a first look into the existing flow topology around ex-Gaston's pouch. Figure 3.5 shows the horizontal flow fields and calculated dividing streamlines at 1800 UTC 02 September from ECMWF analysis data at 500, 700, 850, and 925 hPa levels when dry air was greatly impacting the pouch.

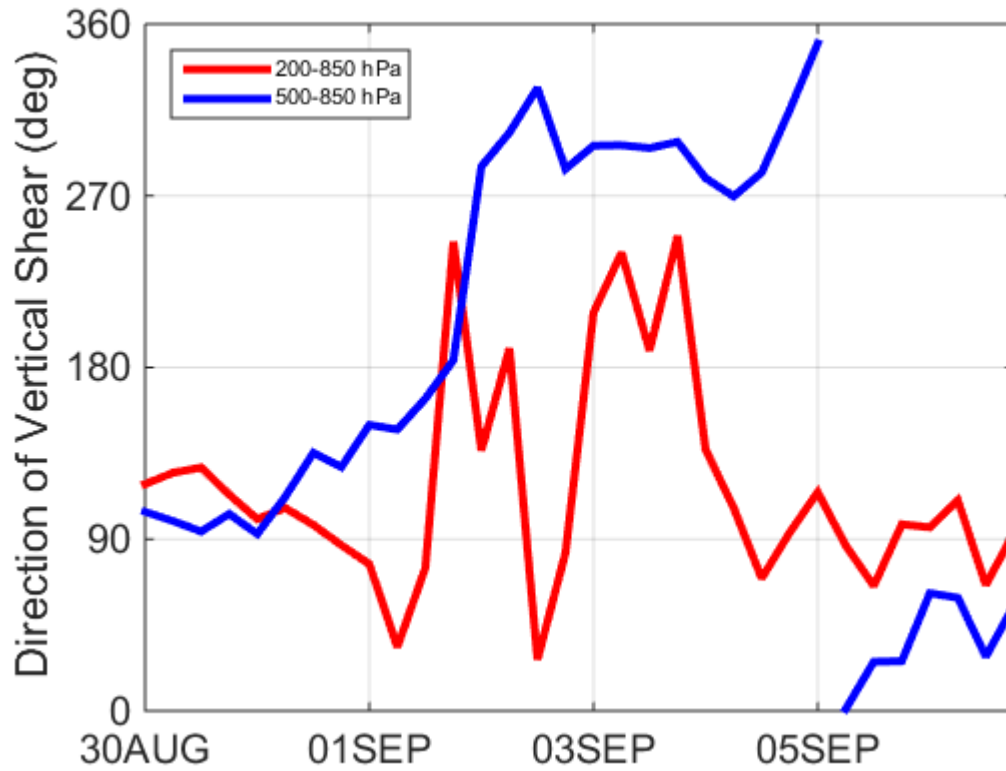


Figure 3.3: Direction of vertical shear analyzed over a  $3^\circ \times 3^\circ$  box centered on the moving sweet spot location. The vertical wind shear is shown for the 200-850 hPa (red line) and the 500-850 hPa (blue line) levels. The directions are compass directions and in a meteorological sense (e.g.,  $90^\circ$  corresponds to easterly shear). The 500-850 hPa shear is mainly from the north on 02 September 2010. Analysis by RM12 shows that is a source region for dry air.

At 700, 850, and 925 hPa, a hyperbolic point lies east of the circulation center. However, to the west of the circulation center, the pouch is open to the environment; thereby providing a pathway for air parcels to enter the pouch (i.e., an “open pouch”). At 500 hPa the hyperbolic point is northwest of the circulation center, and the pouch is open to the east. This interpretation is consistent with the study of RM12 who performed a more comprehensive study of the flow topology of ex-Gaston. In particular, RM12 analyzed Lagrangian coherent structures derived from particle trajectories, and found that lateral, dry air intrusion occurred from 01 to 05 September (RM12 Figure 6 therein). These current findings at 700, 850, and 925 hPa are consistent with the detailed Lagrangian analysis of ex-Gaston



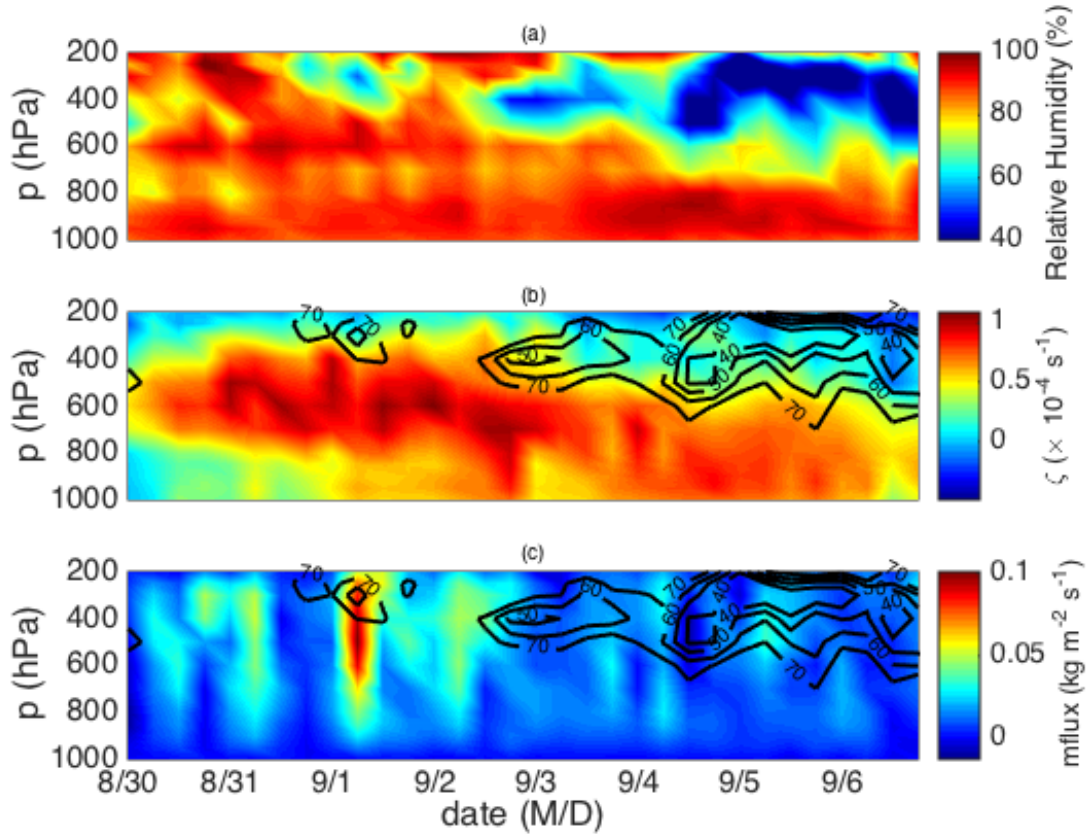


Figure 3.4: Time-height cross-section of system averaged quantities within a  $3^\circ \times 3^\circ$  box from 0000 UTC 30 August to 1800 UTC 06 September. (a) Relative humidity in percent. (b) Relative vorticity ( $\zeta$ ) with relative humidity contours of 40, 50, 60, and 70%. (c) Vertical mass flux with relative humidity contours of 40, 50, 60, and 70%. A dry layer near and above 600 hPa appears on 02 September and persists through 06 September. There are corresponding decreases in relative vorticity and mass flux after 02 September.

by RM12.

The structure of the pouch can be further studied by looking at the time-dependent nature of the flow by calculating hyperbolic trajectories (Samelson and Wiggins 2006). Hyperbolic trajectories are trajectories of the time-dependent flow field that share the same linear stability properties as hyperbolic fixed points in time-independent flow. These hyperbolic trajectories have stable and unstable manifolds associated with them, and these manifolds control particle transport in time-dependent flow (Ide et al. 2002).

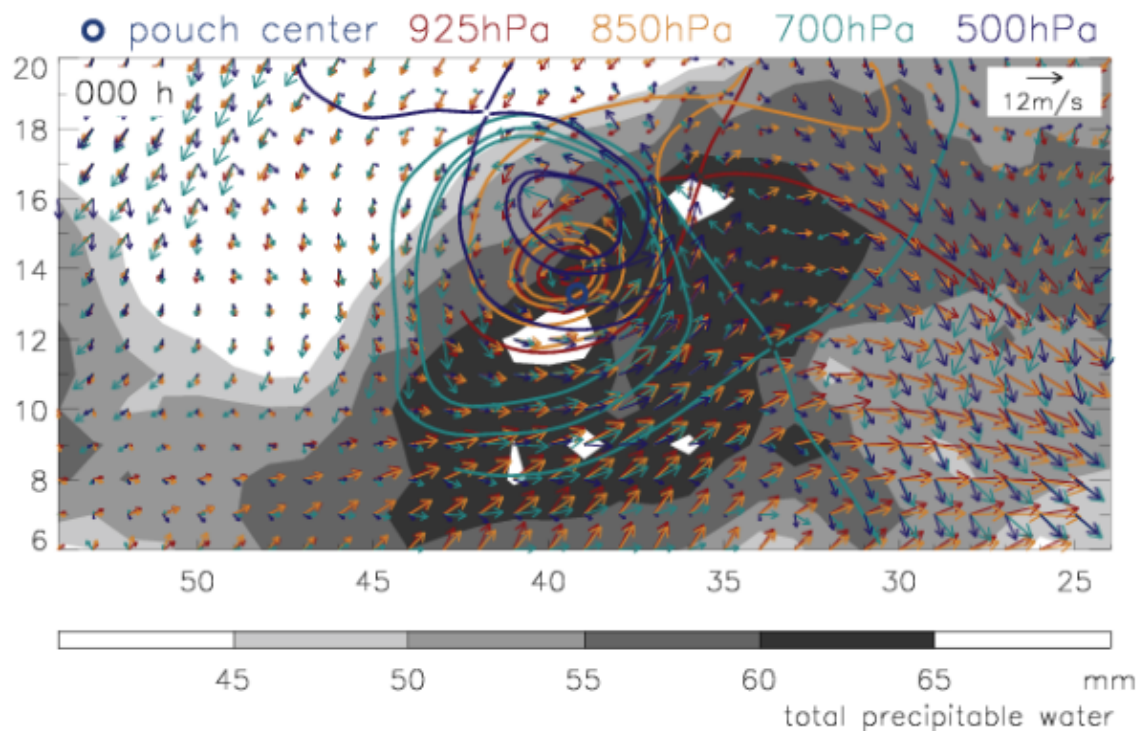


Figure 3.5: Dividing streamlines at 1800 UTC 02 September 2010. Dividing streamlines are shown for 500, 700, 850, and 925 hPa, and are overlaid on co-moving wind vectors at each level and total precipitable water.

Figure 3.6 shows a time sequence of stable and unstable manifolds at 500 hPa (left column) and 700 hPa (right column) from 0000 UTC 01 September to 0000 UTC 03 September. Stable manifolds are indicated with red lines, and unstable manifolds are indicated with blue and cyan lines. For reference, a 3-degree radius circle around ex-Gaston's diagnosed pouch center is indicated by the green circle. Throughout this 48-hour period, the stable manifold (red line) and an unstable manifold (blue line) intersect east of ex-Gaston's pouch on the 500 and 700 hPa pressure surfaces. The intersection of these manifolds marks the location of a hyperbolic trajectory, and the persistence of these manifolds is indicative of the pouch having a barrier to intrusions from the northeast, east and southeast. In this case the manifolds comprise only part of a cat's eye. At 700 hPa, the stable (red line) manifold also intersects the unstable (cyan line) manifold south of ex-Gaston's pouch. This second intersection is not evident on the 500 hPa pressure level. At both the 500 hPa and 700 hPa levels, there are no intersecting manifolds west of the pouch. No intersection implies

no additional hyperbolic trajectory, and leaves no way for boundaries to be topologically connected into a separatrix.<sup>1</sup> While there is a difference between the dividing streamline and Lagrangian manifold analyses at 500 hPa, the two methods are consistent at the other pressure levels presented. The Lagrangian manifold method is more complete and accurate by incorporating the time-dependent nature of the analyzed flow.

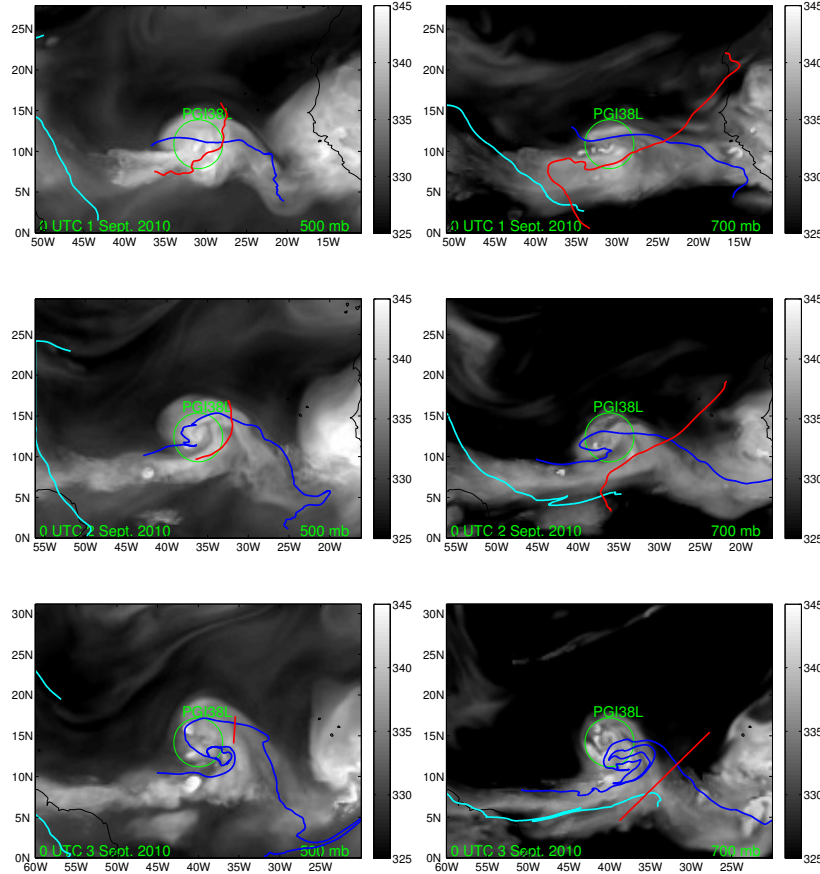


Figure 3.6: Lagrangian manifolds are overlaid on  $\theta_e$  fields at 500 hPa (left column) and 700 hPa (right column) from 01 to 03 September. Stable manifolds are in red, and unstable manifolds are in blue and cyan. The abscissa is longitude and ordinate is latitude. The manifolds indicate that the pouch had a hyperbolic point to the east, but was open to environmental air to the west (figure provided by B. Rutherford, personal communication).

<sup>1</sup>A separatrix is a flow partitioning boundary formed by connected segments of manifolds or material curves.

To identify the source region for the dry air that entered ex-Gaston’s pouch at 700, 600, 500, and 400 hPa on 1800 UTC 02 September, backward trajectories were computed for particles seeded within a 3-degree radius of the pouch center. Trajectories were computed as in RM12 using a fourth-order Runge-Kutta method with a 15-minute intermediate time step and bi-cubic interpolation in both time and space on constant pressure surfaces. At 400 hPa, particles that are within a 3-degree radius of the pouch at 1800 UTC 02 September originated to the north of the pouch (Figure 3.7). At the 500 hPa level, particles that are within a 3-degree radius of the pouch at 1800 UTC 02 September originated primarily northeast and southwest of the pouch (Figure 3.8).

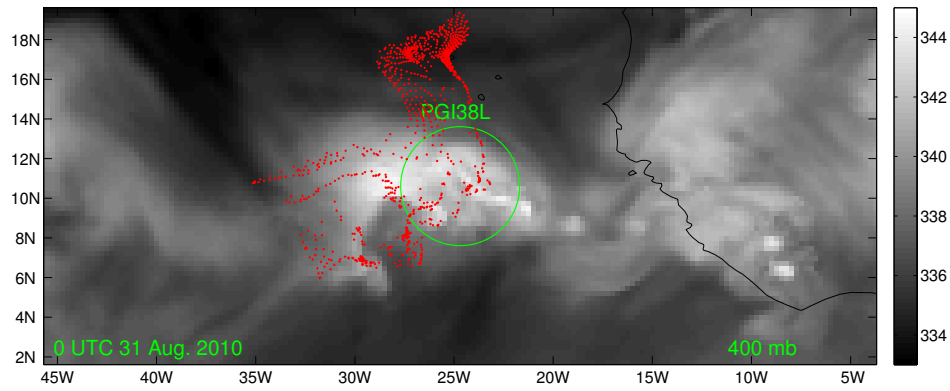


Figure 3.7: Particle trajectory locations at 400 hPa 1800 UTC 31 August are overlaid on  $\theta_e$  (K). These trajectories are all within a radius of 3 degrees of the pouch center (green circle) by 1800 UTC, 02 September. The abscissa is longitude and ordinate is latitude (figure provided by B. Rutherford, personal communication).

For the trajectories identified in the foregoing figures, it is of interest to document the evolution of pseudo-equivalent potential temperature,  $\theta_e$ . For a moist air parcel,  $\theta_e$  is approximately materially conserved in the absence of mixing processes. On a given pressure surface,  $\theta_e$  is a function of moisture and temperature and because of its tracer-like property

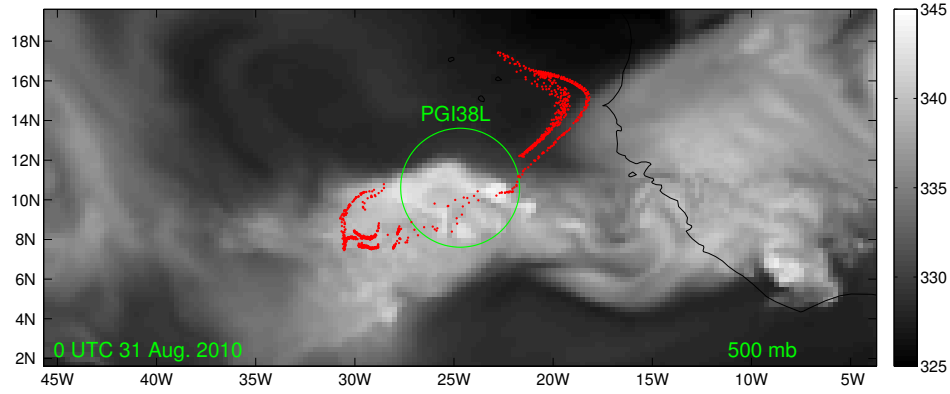


Figure 3.8: Particle trajectory locations at 500 hPa 1800 UTC 31 August are overlaid on  $\theta_e$  (K). These trajectories are all within a radius of 3 degrees of the pouch center (green circle) by 1800 UTC 02 September. The abscissa is longitude and ordinate is latitude (figure provided by B. Rutherford, personal communication).

and weak temperature gradient in the tropics, increases or decreases in  $\theta_e$  along a constant pressure trajectory reflect primarily changes in moisture. For all calculations presented here, the  $\theta_e$  definition as given by Bolton (1980) (his Eq. (43)) is used.

Figure 3.9 summarizes the evolution of  $\theta_e$  for the trajectories identified previously in Figure 3.8 on the 500 hPa level. A colored point in the figure represents a snapshot of the particular particle's  $\theta_e$  and radial distance from the center of Gaston's pouch. The colors range from brown to blue, with brown denoting the earliest time of 0000 UTC 31 August and blue denoting the latest time of 1800 UTC 2 September. The quasi-regular pattern of blue dots between 0 and 3 degrees radius is a manifestation of the initial seeding method for the backward trajectory calculation.

Figure 3.9 shows that particles seeded within the nominal pouch radius of 3 degrees originate from two distinct source regions (brown points) outside of the pouch. The two source

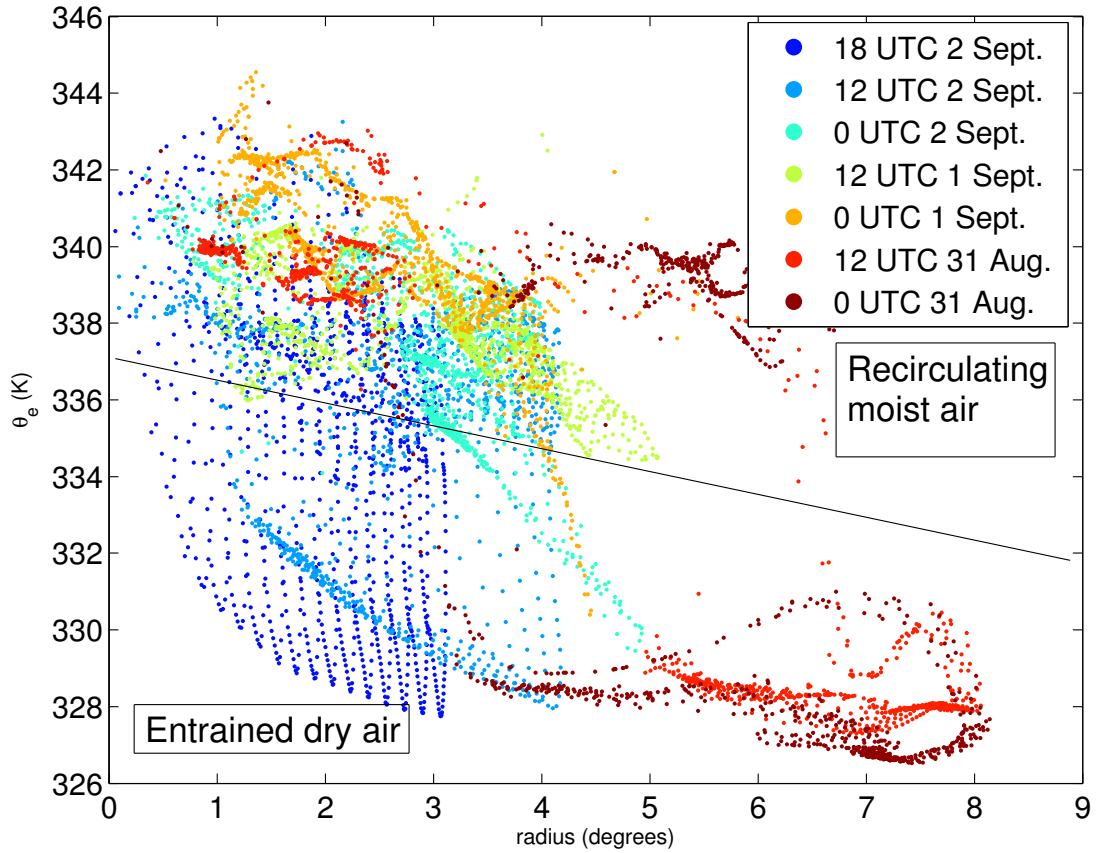


Figure 3.9:  $\theta_e$  vs. radial distance from the center of ex-Gaston's pouch. The colors range from brown to blue, with brown denoting the earliest time of 0000 UTC 31 August and blue denoting the latest time of 1800 UTC 02 September (figure provided by B. Rutherford, personal communication).

regions are indicated by the red dots in Figure 3.8; one source region is located in an arch-like filament northeast of the pouch in a dry (low  $\theta_e \sim 328$  K) environment; the other is located west and southwest of the pouch in a relatively moist environment ( $\theta_e \sim 339$  K). As these particles enter ex-Gaston's pouch from 0000 UTC 31 August to 1800 UTC 02 September, the moist particles remain relatively moist, and the dry particles remain relatively dry. The black slanted line in Figure 3.9 approximately differentiates these moist and dry trajectory paths, and its shallow slope indicates that dry air was not significantly moistened before entering the pouch. A similar analysis was performed for the 400 hPa level (not shown), and showed similar trends as the 500 hPa level. These results demon-

strate that dry air was entering Gaston’s pouch during this 66 hour period from 0000 UTC 31 August to 1800 UTC 02 September.

### **3.2 Implications of Dry Air and a Degraded Pouch**

The findings from the previous section showing dry air entering ex-Gaston’s pouch motivate an important question in its non-redevelopment: What was the role of dry air in the non-development? To understand the role of the dry air entering the pouch it is useful to review previous studies of the role of dry air on convection. A new hypothesis on the role of dry air in tropical cyclogenesis was articulated in the work of Smith and Montgomery (2012). The authors studied the convective environments of the tropical disturbances during the PREDICT experiment. They found that a prominent difference between developing and non-developing disturbances was the difference in  $\theta_e$  between the surface and 3 km. Smith and Montgomery (2012) hypothesized that entrained, dry air weakens the convective updraughts and thereby weakens the vortex-tube stretching of ambient and local cyclonic vorticity. Weakening of the convective updraughts implies a frustrated vorticity amplification process. The hypothesis of Smith and Montgomery (2012) stands in contrast to the traditional notion that dry air increases the strength of convective downdraughts and increases the low-level divergence that accompanies these downdraughts.

In another study of convective environments, James and Markowski (2010) investigated the role of dry air aloft on deep convection. In their numerical study, they found in the low CAPE environments ( $1500 \text{ J kg}^{-1}$ ) with a dry air layer of  $\text{RH}=70\%$  near 700 hPa, the updraught mass flux was reduced throughout the depth of the troposphere, and the downdraught mass flux was either unchanged or reduced.

In a related study, Kilroy and Smith (2012) (hereafter referred to as KS12) used a high-resolution cloud model to examine the role of dry air on rotating deep convection in tropical cyclogenesis. KS12 created an idealized sounding based on the ex-Gaston environment, and proceeded to modify the idealized sounding by injecting dry air into the mid-levels. They found through a series of experiments (summarized in their Table 2) that dry air aloft reduced the convective updraught strength and the vertical extent of the convective updraught.

KS12 also used a “moist” and a “dry” profile from the PREDICT Experiment. The moist



profile was from 1820 UTC 05 September, and had a total precipitable water (TPW) of  $65.2 \text{ kg m}^{-2}$ . The dry profile was from 1448 UTC 05 September, and  $\text{TPW}=43.5 \text{ kg m}^{-2}$ . In the moist environment, KS12 found maximum convective updraught and downdraught velocities of  $34$  and  $10.9 \text{ m s}^{-1}$ , respectively, and vertical extent above  $10 \text{ km}$ . However, in the dry environment the maximum updraught velocity and downdraught velocities were  $11.4$  and  $6.3 \text{ m s}^{-1}$ , respectively, and the vertical extent was only  $\sim 7 \text{ km}$  (Figure 3.10)). Dry air reduced both the updraught and the maximum vertical extent, while the downdraught velocities were only moderately reduced, consistent with findings from the experiments with the idealized soundings. These results showed that dry air reduces cloud buoyancy, thus making mass flux profiles weaker and shallower than in a moist environment, as well as making the convective updraught less effective in amplifying vertical vorticity over a deep tropospheric layer (Smith and Montgomery 2012).

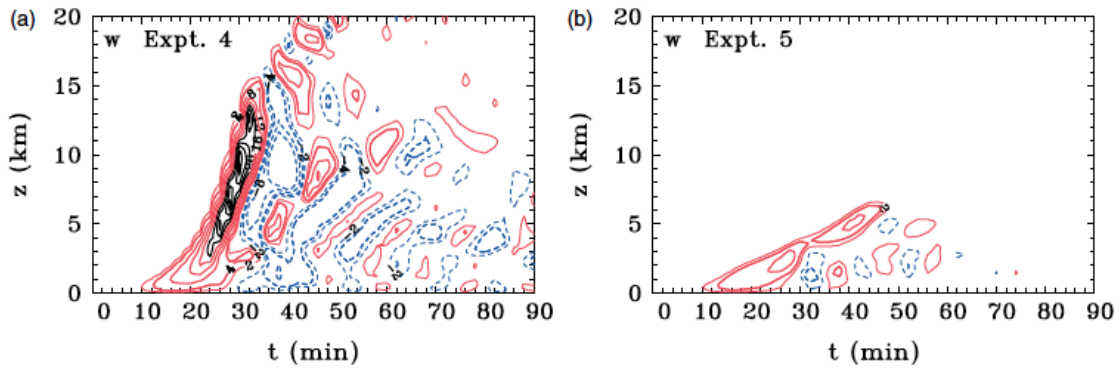


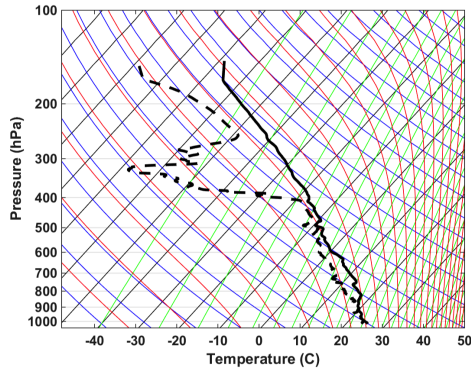
Figure 3.10: Height-time series of maximum vertical velocities from the numerical experiments of KS12 using the (a) moist profile and the (b) dry profile from PREDICT. Red lines are positive (updraught) and blue-dashed lines are negative (downdraughts). Thin contours are  $2 \text{ m s}^{-1}$  and thick contours are  $4 \text{ m s}^{-1}$ . Thick black contours indicate values above  $20 \text{ m s}^{-1}$  in  $5 \text{ m s}^{-1}$  intervals (from KS12).

The PREDICT data from 02 September are compared to the PREDICT data used by KS12 (Figure 3.11). The moist profiles (Figures 3.11a and 3.11b) are from within the pouch, and show a moist environment in a layer from the surface to  $400 \text{ hPa}$ , and shallow, dry layer between  $\sim 300 - 400 \text{ hPa}$ . From KS12, the moist sounding has  $\text{CAPE} = 3498 \text{ kg m}^{-2}$ ,  $\text{CIN} = 0 \text{ kg m}^{-2}$ , and  $\text{TPW} = 65.2 \text{ kg m}^{-2}$  (Smith and Montgomery 2012). A typical moist sounding from 02 September has  $\text{CAPE} = 1566 \text{ kg m}^{-2}$ ,  $\text{CIN} = 0 \text{ kg m}^{-2}$ , and  $\text{TPW} = 59.9$

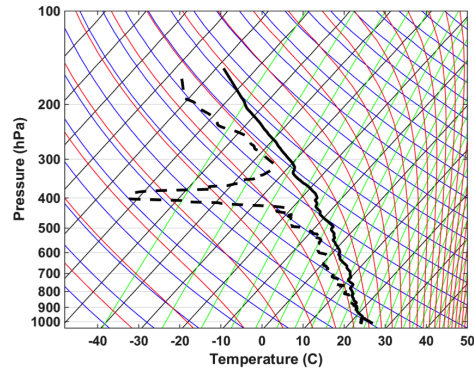


$\text{kg m}^{-2}$  (Smith and Montgomery 2012).

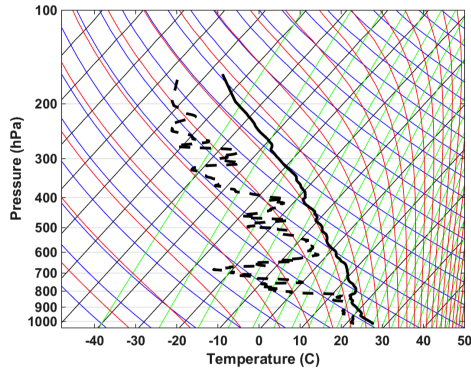
The dry profiles (Figures 3.11c and 3.11d) were taken outside of ex-Gaston's pouch. They both show a shallow moist layer below  $\sim 800$  hPa, and dry through a deep layer above 800 hPa. From KS12, the dry sounding has  $\text{CAPE} = 1145 \text{ kg m}^{-2}$ ,  $\text{CIN} = 21 \text{ kg m}^{-2}$ , and  $\text{TPW} = 43.5 \text{ kg m}^{-2}$  (Smith and Montgomery 2012). A typical dry sounding from 02 September has  $\text{CAPE} = 525 \text{ kg m}^{-2}$ ,  $\text{CIN} = 75 \text{ kg m}^{-2}$ , and  $\text{TPW} = 35.6 \text{ kg m}^{-2}$  (Smith and Montgomery 2012). From the similarities in these profiles, one would expect similar results for 02 September as KS12 found for 05 September data (discussed above).



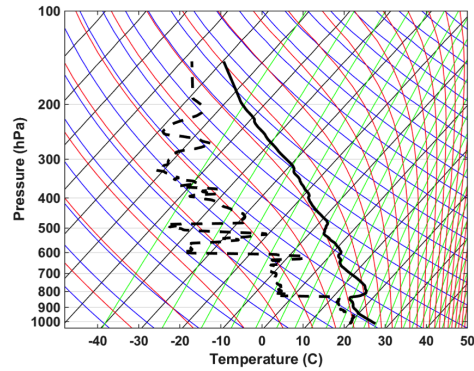
(a) 1820 UTC 05 September



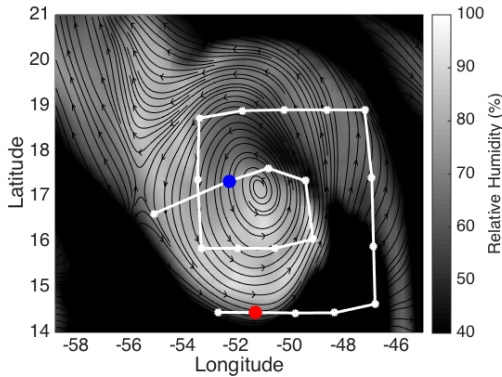
(b) 1713 UTC 02 September



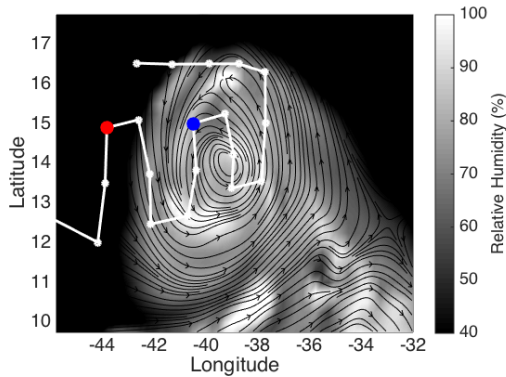
(c) 1448 UTC 05 September



(d) 1818 UTC 02 September



(e) Research Flight 11: 05 September



(f) Research Flight 09: 02 September

Figure 3.11: Comparison for moist (a) and dry (c) soundings from 05 September used by KS12 with typical moist (b) and dry (d) soundings from 02 September. Solid lines indicate temperature and dashed-lines indicate dew point temperature. Flight paths (white) for 05 September (e) and 02 September (f) are overlaid on the RH field at 700 hPa (shading) and co-moving streamlines (black lines). Blue and red dots indicate the locations of the selected moist and dry soundings, respectively, for each day.

In total, the foregoing results suggest that the pouch was vulnerable to the environment with dry air penetrating the pouch and disrupting the amplification of vorticity. This analysis of the kinematic, dynamic, and thermodynamic structure of ex-Gaston in the ECMWF analysis, as well as the work of RM12 and Davis and Ahijevych (2012, Figure 9 therein), show that ex-Gaston's pouch was misaligned, and vulnerable to environmental air as early as 02 September (Figure 3.4), the day of the first PREDICT research flight into this remnant low. This dry air results in divergence near the 600 hPa level, thus causing an expanding circulation loop at these levels. From Kelvin's circulation theorem, as the loop expands the absolute vertical vorticity must decrease in order to conserve absolute circulation. A reduction in vorticity will create a compromised pouch, which will allow further intrusion of dry air and inhibit vorticity amplification.

GR14 propose a different process that leads to the failed redevelopment of ex-Gaston. GR14 (p. 3076) hypothesize that the "severe decrease of the mid-level vortex observed between the period of Gaston 1 (02 September) and Gaston 2 (03 September) was a deciding factor for Gaston's failure to re-intensify." It is important to note that GR14, RM12, and Davis and Ahijevych (2012) agree on the decay of the mid-level vortex. GR14 hypothesize that convection was suppressed by a strong trade wind inversion, and attribute the decrease in the mid-level vorticity to this strong trade inversion and corresponding structure of the vertical mass flux profile. GR14 argue that the trade wind inversion air causes the decrease in magnitude with height of the mass flux profile. However, this study contends that the intrusion of dry air at and above the 600 hPa level is responsible for the decrease in the mass flux profile.

To address the hypothesized influence of the strong trade wind inversion, it proves useful to review the thermodynamic structure of the dropsonde data collected on 02 September. The PREDICT experiment released 19 dropsondes in ex-Gaston on this day. GR14 included drop numbers 2 through 14 (see Table 3.1) in their 3DVAR analysis and area-averaging schemes. Within their  $4^\circ \times 4^\circ$  analysis box (their Figure 8), only one drop (drop number 2, located northwest of ex-Gaston's pouch) shows clear evidence of a temperature inversion (Figure 3.12), while 11 of the profiles show evidence of a dry layer above 600 hPa. It is unclear how one particular sounding could have such a hypothesized impact on the system-scale vorticity dynamics.

Table 3.1: Summary of Dropsondes from PREDICT Research Flight 9 (RF09) on 02 September (after Smith and Montgomery 2012).

Drop Num.	Time (UTC)	TPW ( $\text{kg m}^{-2}$ )	CAPE ( $\text{J kg}^{-1}$ )	CIN ( $\text{J kg}^{-1}$ )
1	1532	33.0	478	149
2	1544	48.2	196	95
3	1555	53.6	24	142
4	1605	61.1	688	6
5	1614	62.8	706	0
6	1624	57.5	1047	9
7	1637	58.4	612	29
8	1647	63.0	1707	0
9	1654	65.9	654	11
10	1703	67.1	1649	0
11	1713	59.9	1566	0
12	1723	57.5	605	5
13	1733	56.7	2	158
14	1745	55.3	0	328
15	1755	53.8	114	110
16	1808	51.1	1155	14
17	1818	35.6	525	75
18	1830	36.1	285	143
19	1843	38.2	101	155

A study of GR14 suggests that these authors appeared to overlook the implications of Davis and Ahijevych (2012) findings of a vertically sheared pouch and RM12’s findings of dry air mixing into ex-Gaston’s pouch between 01 and 03 September (RM12’s Figure 6), a time period spanning the first day of PREDICT observations (02 September). While GR14 acknowledge the role of a transient flow component in causing a reversal in the sign of the vorticity tendency, they do not recognize the role of this component in modulating the transport of dry air into ex-Gaston. Thus, GR14 appear also to misinterpret the results of Smith and Montgomery (2012) and RM12: GR14 (p. 3076-3077) imply that ex-Gaston’s pouch was “robust” (i.e., closed) on 02 September, and therefore unlikely that “dry air might have been drawn into the core of Gaston.”

The offered hypothesis of Gaston’s non-redevelopment described above stands somewhat

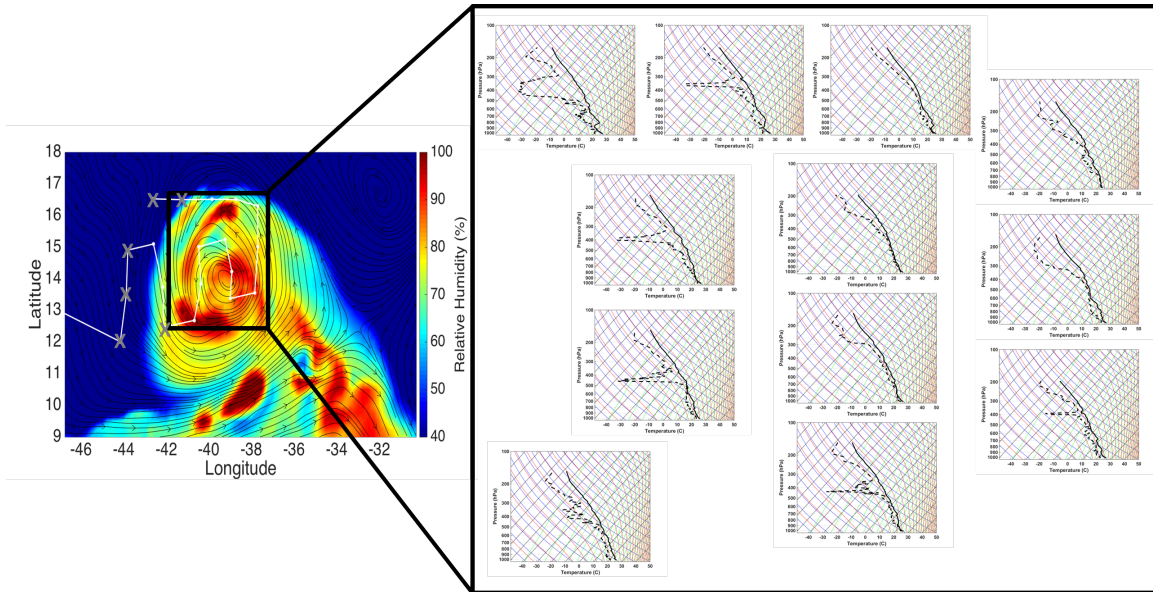


Figure 3.12: PREDICT flight path and dropsonde locations (white line with white points) overlaid on 700 hPa relative humidity (shading) and co-moving streamlines from ECMWF analysis data at 1800 UTC 02 September. The gray Xs indicate locations where dropsonde data show evidence of an inversion. The black box corresponds to GR14 Figure 8. The expanded box shows the skew T - ln P diagrams from the 02 September PREDICT flight dropsondes within the GR14 area of interest. Only the profile in the northwest corner in the black box shows evidence of an inversion.

in contrast to the alternative hypothesis by Gjorgjievska and Raymond (2014). The data shown herein supports the view that dry air penetrated the pouch before the first flight into ex-Gaston and disrupted the amplification of vorticity at those levels where dry air intruded. GR14 agree with this hypothesis of a compromised pouch and dry air intrusion, but only after 04 September.

The data from PREDICT research flight 9 on 02 September does show evidence for an inversion outside the GR14 analysis box for ex-Gaston's pouch (Figure 3.12). To investigate the influence of the dry, trade inversion air west of ex-Gaston's pouch on 02 September, a forward trajectory analysis (Figure 3.12, grey Xs west of the black box) was performed. Particles were seeded on the 850 hPa pressure level west of the sweet spot (where the PREDICT data show a temperature inversion) at 1200 UTC 02 September and integrated forward to 0000 UTC 04 September. Nearly all of the particles are located outside of a 3

degree radius of the pouch center by 0000 UTC 04 September. This analysis shows that the observed dry, trade inversion air on 02 September does not enter the pouch, and has little influence on the non-development of ex-Gaston.

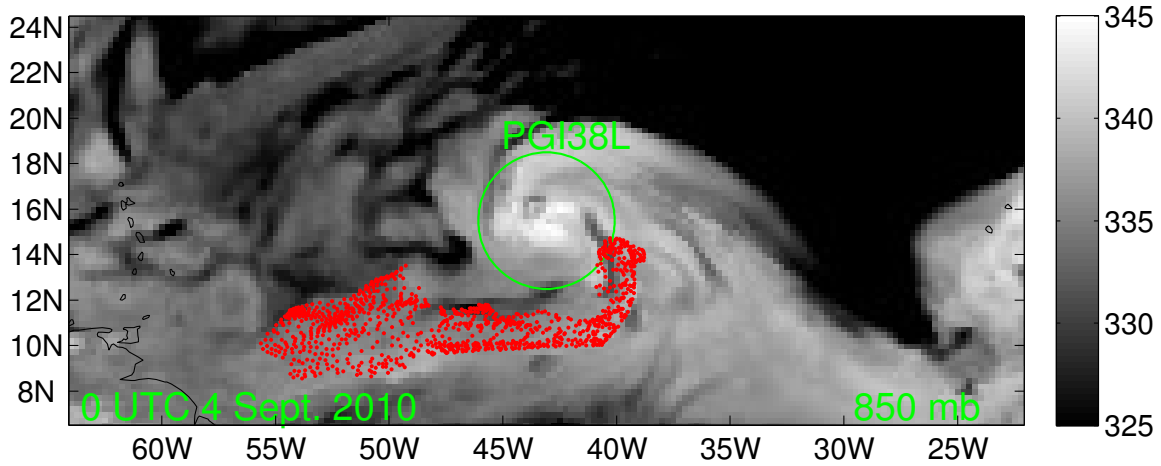


Figure 3.13: Particle trajectory locations at 850 hPa at 0000 UTC 04 September overlaid on  $\theta_e$  (K). Particles were seeded west of ex-Gaston's pouch at 1200 UTC 02 September, within a suspected trade wind inversion layer. These trajectories are all outside of a 3 degree radius of the pouch center (green circle) on 04 September. The abscissa is longitude and ordinate is latitude (figure provided by B. Rutherford, personal communication).

---

## CHAPTER 4:

### The Development of Hurricane Karl

---

Hurricane Karl developed within a region of the intertropical convergence zone (ITCZ) near the northern coast of South America. Southwesterlies off the continent helped to enhance the ITCZ and increase convection between 50° and 60° W on 08 September (Montgomery et al. 2012). An easterly wave formed near this enhanced region of the ITCZ and continued to propagate westwards into the Caribbean. The tropical low strengthened to a tropical storm on 2100 UTC 14 September, and made landfall along Mexico's Yucatan coast. Karl then strengthened to a category 3 hurricane over the Bay of Campeche on 17 September, and made landfall near Vera Cruz, Mexico (Figure 4.1). Although there was

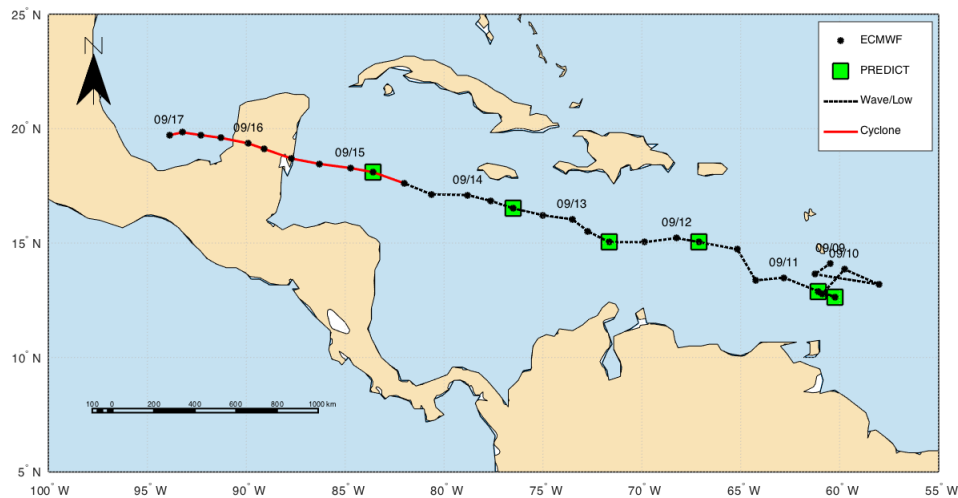


Figure 4.1: Track for Karl based on pouch center (black dots) as identified in the 6 hour, ECMWF analysis data. Green squares show approximate times of PREDICT research flights over the disturbance. The red line indicates when the National Hurricane Center designated the disturbance as at least a tropical depression. The black-dashed line indicated when the disturbance was an incipient wave or remnant low.

recurrent deep, mesoscale convection in and around the pre-Karl disturbance, it was not until approximately 1200 UTC 14 September that there was organized and persistent deep



convection to support the transition of the pre-Karl wave-pouch disturbance into a tropical cyclone. Figure 4.2 summarizes the evolution of the convection associated with Karl's development.

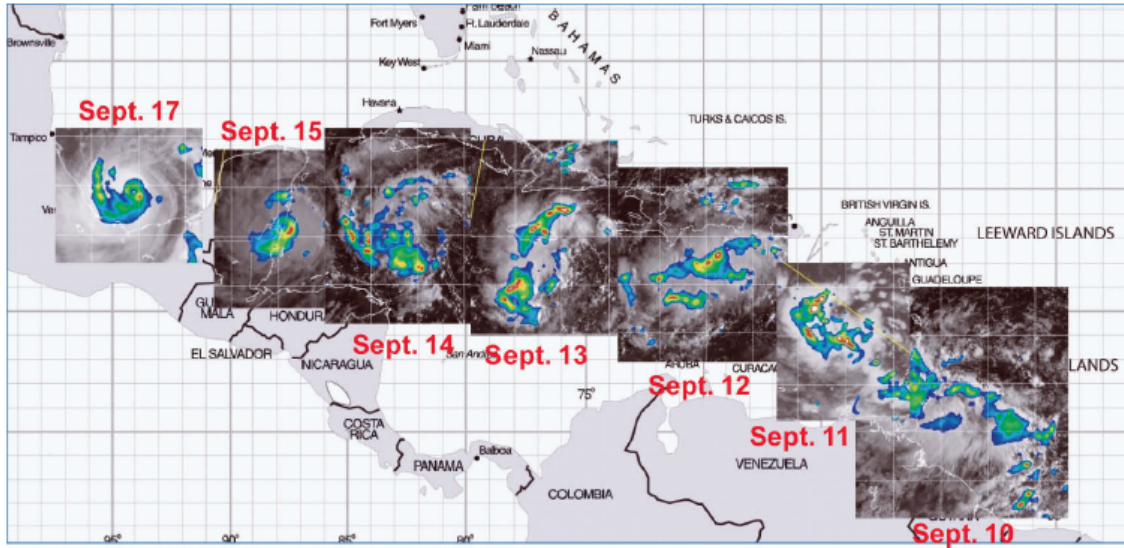


Figure 4.2: 85 GHz montage for Karl's track from 10 to 17 September. Warmer colors indicate active convection (from Montgomery et al. 2012).

Despite favorable conditions for tropical cyclone formation, Karl's development was not a forgone conclusion. PREDICT mission scientists observed periods of deep convection that nearly coincided with the diurnal cycle (Davis 2010a,b). Davis and Ahijevych (2012) presented a time-radius diagram of cloud-top temperatures derived from Geostationary Operational Environmental Satellite (GOES) IR data during Karl's development (Figure 4.3). This data indicates that cold cloud signature decreases simultaneously at all radii. Davis and Ahijevych (2012) notes that the convection (or cold cloud signature) initiates between 1200 and 1500 UTC. These times correspond to the diurnal peak in convection for the Caribbean (Hirose et al. 2008; Sorooshian et al. 2002). After genesis, Figure 4.3 shows there is a persistent cold cloud signature extending to a radius of  $\sim 150$  km (Davis and Ahijevych 2012).



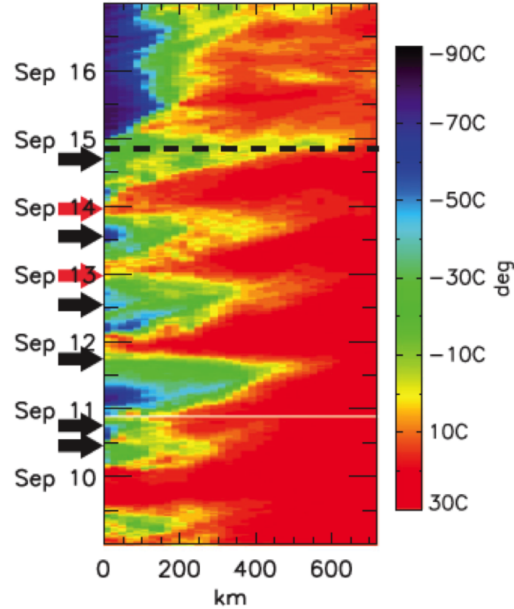


Figure 4.3: Time-radius diagram of cloud-top temperatures derived from GOES IR data. Temperatures are the 75th percentile temperature within each radial ring of 20 km. The dashed line indicates the time of genesis. The black arrows indicate the times of GV PRE-DICT flights and the red arrows indicate times of research flights by NOAA or NASA (from Davis and Ahijevych 2012).

## 4.1 Pre-Karl's Environment

This analysis of Karl's genesis begins by characterizing its development environment. Similar to the ex-Gaston analysis, the "Deep-layer shear" and "pouch shear" are computed by taking the vector differential of horizontal winds between the 200 hPa and 850 hPa levels, and between the 500 hPa and 850 hPa levels, respectively, averaged over a  $3^\circ \times 3^\circ$  box centered at the pouch center. The pouch-scale averaging is performed on a  $3^\circ \times 3^\circ$  box, centered on the circulation center as defined by the 700 hPa tracking level.

The pouch shear remains low ( $\sim 2\text{--}8 \text{ m s}^{-1}$ ) from 09 to 17 September. The deep-layer shear is similar to the pouch scale, except for a period from 0000 UTC 10 September to 1200 UTC 11 September when the magnitude of vertical shear increases to  $\sim 13 \text{ m s}^{-1}$  (Figure 4.4). For both the deep-layer and pouch shear, the direction is predominantly from the east

and southeast (Figure 4.5). From 1800 UTC 11 September to 1800 UTC 12 September, the direction of the pouch shear rotates clockwise from the east to the west, and then back to the east. These shear results are consistent with the analysis of PREDICT data by Davis and Ahijevych (2012, Figure 10 therein). Karl eventually developed in a favorable, low shear environment.

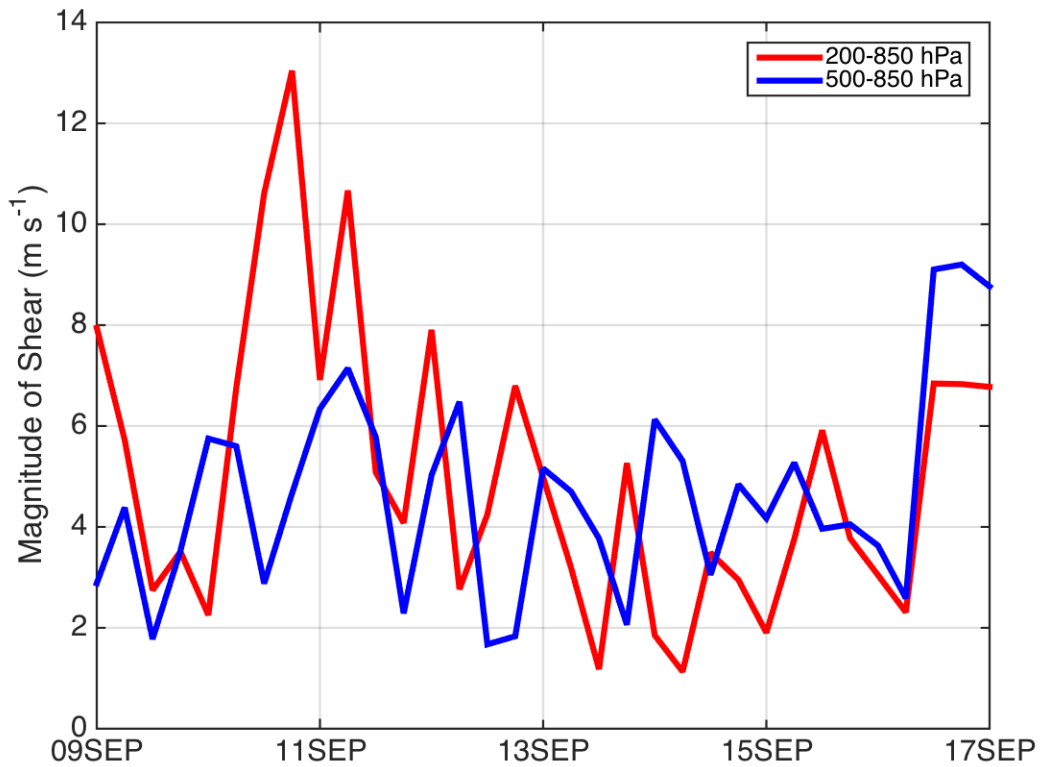


Figure 4.4: Average of vertical wind shear magnitude is shown for the 200-850 hPa (red line) and the 500-850 hPa (blue line) levels.

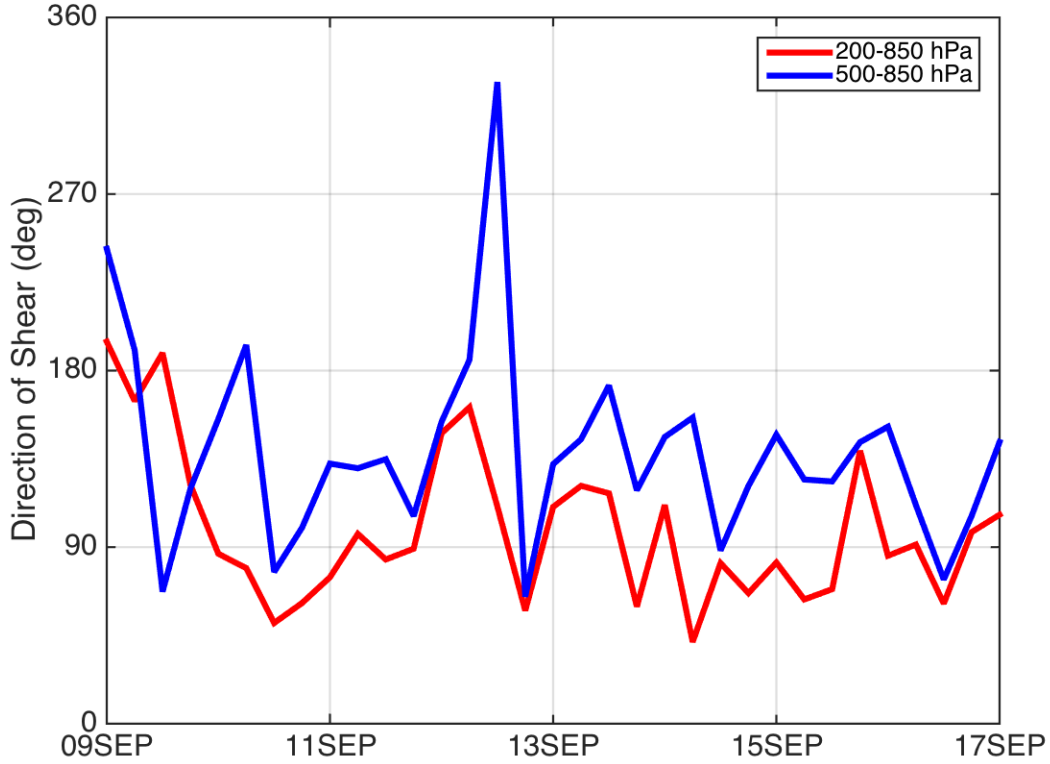


Figure 4.5: Direction of vertical shear analyzed over a  $3^\circ \times 3^\circ$  box centered on the moving sweet spot location. The vertical wind shear is shown for the 200-850 hPa (red line) and the 500-850 hPa (blue line) levels. The directions are compass directions in a meteorological sense (e.g.,  $90^\circ$  corresponds to easterly shear).

The evolution of relative humidity, relative vorticity ( $\zeta$ ), and vertical mass flux is analyzed using time-height Hovmoeller diagrams (Figure 4.6). The quantities were averaged over  $3^\circ \times 3^\circ$  boxes centered on the sweet spot as defined by the 700 hPa tracking level. As in Chapter 3, this analysis uses the model vertical velocity in pressure coordinates,  $\omega$ , to calculate the mass flux as  $\rho w = -\omega/g$ , where  $\rho$  is density,  $w$  is vertical velocity in height coordinates, and  $g$  is the acceleration due to gravity. The relative humidity shows that while there was a dry layer above 600 hPa from 0000 UTC 09 September to 0000 UTC 11 September, pre-Karl was in a moist environment with average relative humidities generally exceeding 80% at all levels. Calculations of  $\theta_e$  (as defined by Bolton 1980, his Eq. 43) averaged over a  $3^\circ \times 3^\circ$  box are a complimentary way to demonstrate that Karl became

more moist throughout the mid-levels from 09 to 14 September (Figure 4.7).

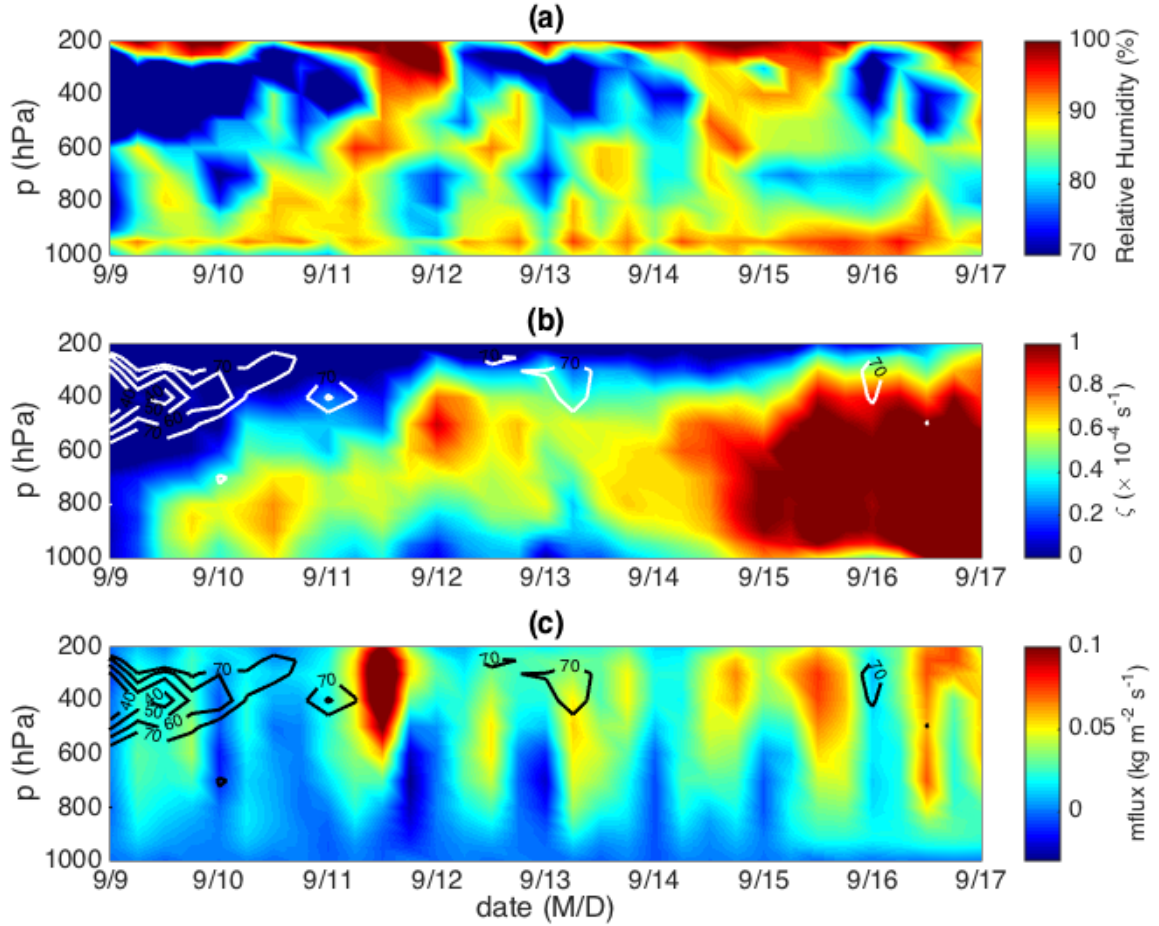


Figure 4.6: Time-height cross-section of system averaged quantities within a  $3^\circ \times 3^\circ$  box from 0000 UTC 09 September to 0000 UTC 17 September. (a) Relative humidity in percent. (b) Relative vorticity ( $\zeta$ ) with relative humidity contours of 40, 50, 60, and 70%. (c) Vertical mass flux with relative humidity contours of 40, 50, 60, and 70%.

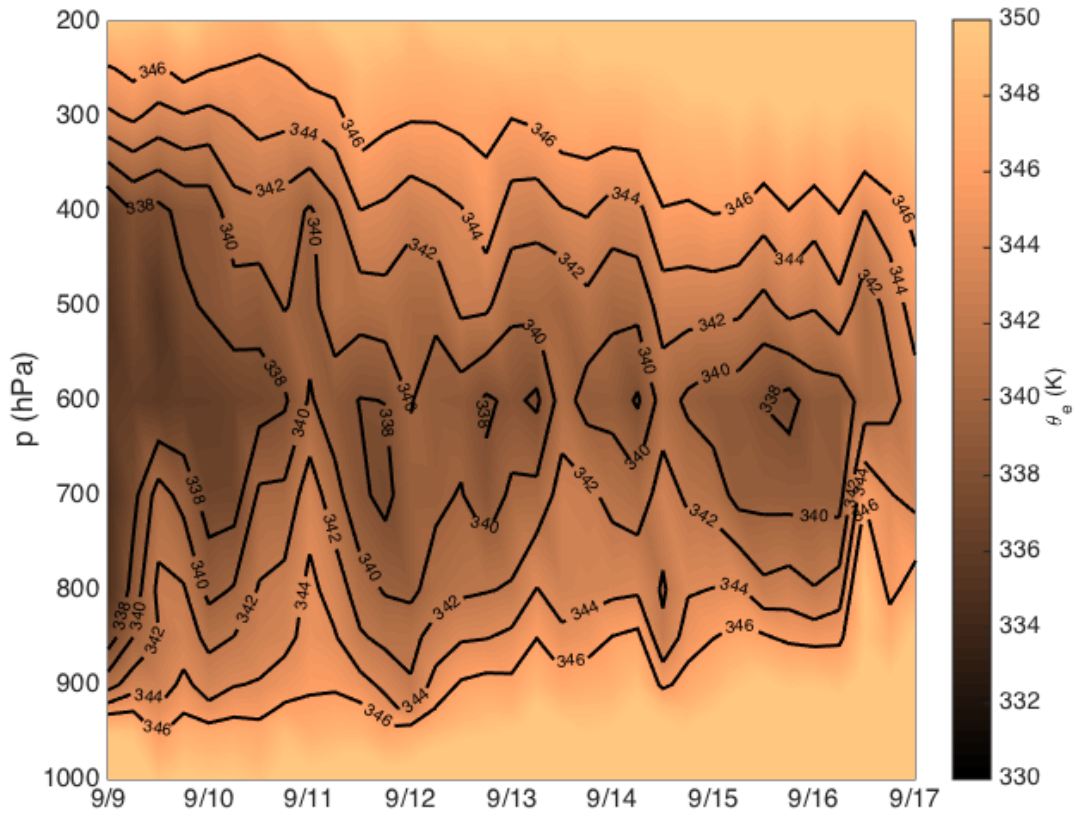


Figure 4.7: Time-height plot of  $\theta_e$  averaged over a  $3^\circ \times 3^\circ$  box from 09 to 17 September. Higher values of  $\theta_e$  indicate greater moisture.

The relative vorticity between 800 and 1000 hPa at 1200 UTC 09 September (Figure 4.6) shows that pre-Karl started to spin-up at these levels. The spin-up extends to the mid-levels (near  $\sim 500$  hPa) by 0000 UTC 10 September. The pre-Karl disturbance then undergoes episodic spin-up and spin-down events before undergoing genesis on 1800 UTC 14 September. At low-levels (850 and 950 hPa), the system spins-down near 0000 UTC 12 and 0000 UTC 13 September (Figure 4.8). The 700 hPa  $\zeta$  is steady from 1200 UTC 10 September to 0000 UTC 13 September. By 1800 UTC 14 September, Karl is spinning-up at all levels.

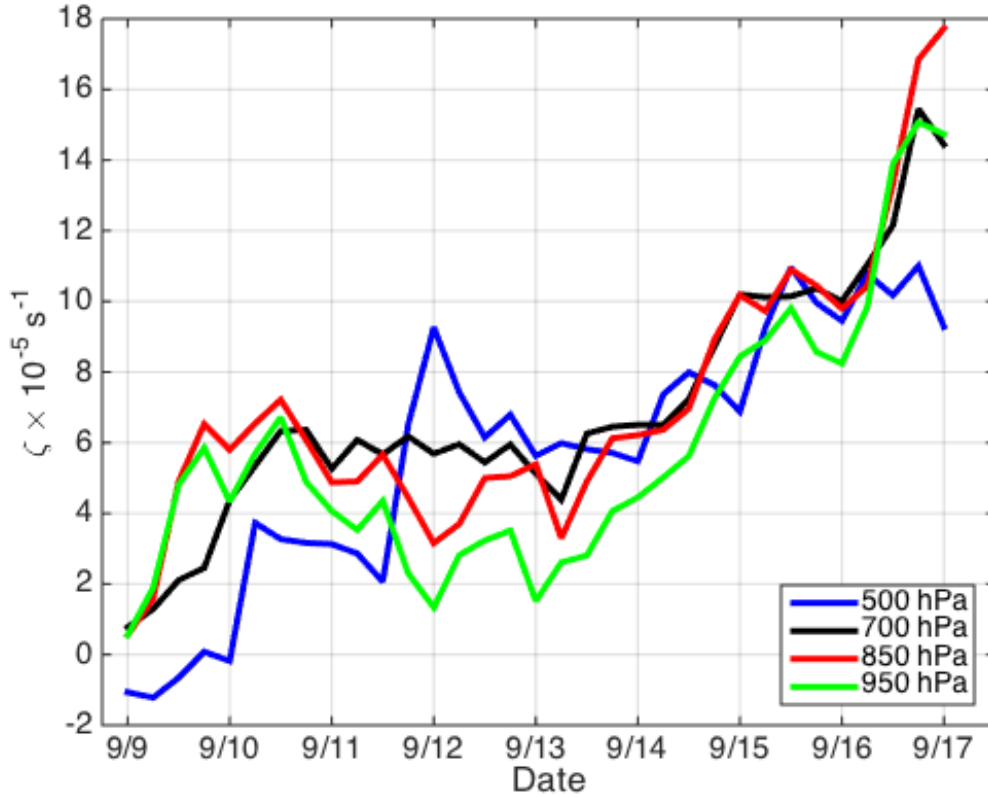


Figure 4.8: Evolution of  $\zeta$  averaged over  $3^\circ \times 3^\circ$  box at the 500, 700, 850, and 950 hPa pressure levels. The time is from 0000 UTC 09 September to 0000 UTC 17 September. Genesis occurred at approximately 1800 UTC 14 September.

In order to investigate the aggregation and amplification of relative vorticity, the distribution of  $\zeta$  was calculated as a function of radius (Figure 4.9). Initially, the  $\zeta$  was averaged over a  $1^\circ \times 1^\circ$  box centered on the tracking level sweet spot (700 hPa).  $\zeta$  was then calculated in concentric square annuli with a  $0.5^\circ$  widths for total box sizes of  $2^\circ \times 2^\circ$  to  $4^\circ \times 4^\circ$ . Wang (2012) noted that averaging  $\zeta$  over pouch scale areas will tend to reduce the calculated magnitude of  $\zeta$ . The averaging scheme used in this calculation is sub-pouch scale and should adequately represent the characteristic distribution of  $\zeta$  as a function of radius. At both the 700 hPa (Figure 4.9a) and 950 hPa levels (Figure 4.9b) there is a moderate amplification of vorticity from 0000 UTC 11 September to 1200 UTC 11 September. At 700 hPa, the pulsing of  $\zeta$  is clear within a box size of  $2^\circ \times 2^\circ$ . The pulsing is much less

pronounced at the 950 hPa level. This could be a result of the averaging algorithm using the 700 hPa sweet spot position to define the box locations for all levels. As discussed by Davis and Ahijevych (2012) and later in this thesis, pre-Karl's pouch was vertically misaligned until late 13 September. Therefore, the box may not be centered on the sweet spot for levels other than the tracking level. However, at 1800 UTC 14 September, there is a rapid amplification of  $\zeta$ . As discussed above, there was persistent, deep convection near pre-Karl's sweet spot at 1200 UTC 14 September, and pre-Karl underwent a transition to a tropical storm by 1800 UTC 14 September.

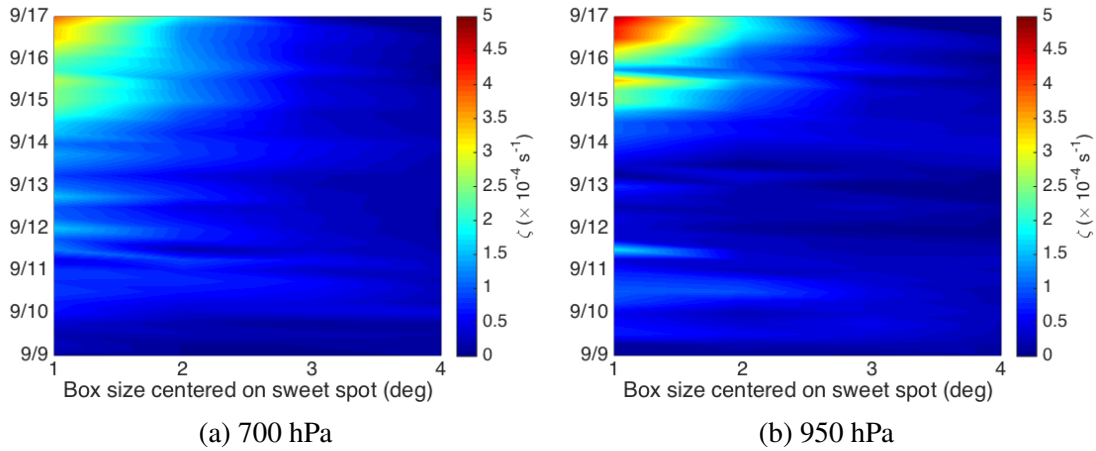


Figure 4.9: Time-radius plots of average  $\zeta$ .  $\zeta$  was averaged over a  $1^\circ \times 1^\circ$  box centered on the 700 hPa (tracking level) sweet spot, and subsequently averaged within  $0.5^\circ$  wide concentric square annuli. Results are shown for the 700 hPa (a) and 950 hPa (b) levels.

The evolution of mass flux (Figure 4.6) shows a pulsing of upward mass flux (warm colors) until the system fully develops into a tropical cyclone. The pulses of upward mass flux are indicative of the intermittent deep convection observed during the PREDICT research flights into this disturbance (Montgomery et al. 2012). Mature mesoscale convective systems (MCS) west of the 900 hPa circulation center (Davis and Ahijevych 2012) support the strong ascent observed in the ECMWF analysis data above 600 hPa at 1200 UTC 11 and 12 September. Sustained, deep convective activity associated with Karl begins at approximately 1200 UTC 14 September.

## 4.2 Circulation and Vorticity Dynamics

Following the treatments of Haynes and McIntyre (1987), Raymond and Lopez-Carrillo (2011), and Lussier III et al. (2014), the equation describing the evolution of vertical vorticity can be written as follows:

$$\frac{\partial \eta}{\partial t} = -\nabla_h \cdot \mathbf{Z} + \hat{\mathbf{k}} \cdot \nabla_h \theta \times \nabla_h \Pi, \quad (4.1)$$

where  $\eta$  is the absolute vertical vorticity ( $f + \zeta$ ), the  $h$  subscript denotes gradients on horizontal surfaces,  $\theta$  is the potential temperature, and  $\Pi$  is the Exner function. The Exner function is defined as  $\Pi = \left(\frac{p}{p_o}\right)^{\frac{R_d}{c_p}}$ , where  $p$  is the pressure,  $p_o$  is a reference pressure,  $R_d$  is the gas constant for dry air, and  $c_p$  is the heat capacity of dry air at a constant pressure. The vorticity flux,  $\mathbf{Z}$ , is defined as (Lussier III et al. 2014):

$$\mathbf{Z} = Z_1 + Z_2 + Z_3 = \eta_z \mathbf{v}_h - \eta_h v_z + \hat{\mathbf{k}} \times \mathbf{F}, \quad (4.2)$$

where a subscript of  $z$  denotes vertical vector components,  $v_h$  are horizontal components of velocity, and  $\mathbf{F}$  represents horizontal friction and other subgrid-scale forcing. The term  $\hat{\mathbf{k}} \cdot \nabla_h \theta \times \nabla_h \Pi$  is the vertical component of the baroclinic generation of vorticity, and is generally neglected because of its small magnitude in the tropics (Raymond and Lopez-Carrillo 2011). In order to obtain an expression for the circulation tendency, one integrates Equation (4.1) (neglecting the relatively small baroclinic generation term) over a horizontal surface area, and uses Gauss's divergence theorem to write:

$$\frac{d\Gamma_a}{dt} = -\oint v_n \eta_z dl + \oint \eta_n v_z dl + \oint F_t dl, \quad (4.3)$$

where  $\Gamma_a$  is the absolute circulation,  $n$  denotes the outward normal component of a vector,  $t$  is the tangential component of a vector, and  $dl$  is line element along a circuit that defines the perimeter of the integration area.

As described in Raymond et al. (2014), the first term of the right hand side of Equation (4.3) represents the net flux of vertical vorticity into the closed loop. The absolute circulation will not change unless there is a convergence of positive vertical vorticity (Figure 4.10, left panel). When this happens, the absolute circulation of the loop (and the area-averaged



vertical vorticity within the loop) will increase with time (Haynes and McIntyre 1987). The second term is a non-advective flux of vertical vorticity, and is commonly referred to as the vortex tilting-like term. This term can change the sign of vorticity (Raymond and Lopez-Carrillo 2011). Upward vertical motion in the region of a horizontal flux of vertical vorticity can distort this surface of equal vorticity upward (Figure 4.10, center panel). This mechanism creates a region of positive vertical vorticity and a region of negative vertical vorticity, and results in a vorticity tendency dipole (Raymond et al. 2014). The third term represents friction (Figure 4.10, right panel) or, for this analysis, any other subgrid-scale forcing in the ECMWF analysis data.

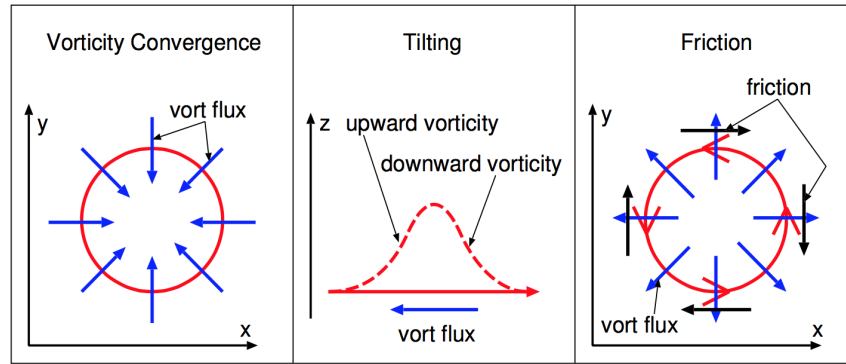


Figure 4.10: Depiction of vorticity fluxes (from Raymond et al. 2014).

In order to understand the circulation tendency and corresponding circulation budget for pre-Karl, the circulation and the advective and non-advective fluxes were calculated on each ECMWF pressure level above and including 950 hPa. Each quantity was calculated and averaged over boxes from  $0.5^\circ$  to  $8.0^\circ$  in  $0.5^\circ$  increments at each 6-hour time step of the ECMWF analysis data. The absolute circulation tendency was calculated by subtracting the previous 6-hour circulation field, from the current circulation field. As an example, the tendency at 1800 UTC 12 September is obtained by subtracting 1200 UTC from 1800 UTC 12 September.

During the development of Karl, there were episodes of spin-up and spin-down at the middle and low-levels (Figures 4.6 and 4.8). As an example, the period from 1800 UTC 11 September to 0000 UTC 12 September shows negative circulation tendency and convergence of absolute vorticity tendency below 700 hPa, but positive tendencies above 700 hPa

(Figure 4.11). From 0000 UTC 12 September to 0600 UTC 12 September, the tendencies are opposite with positive circulation and convergence of absolute vorticity tendencies below 600 hPa, but negative tendencies above 600 hPa (Figure 4.12). The contribution from the non-advective (tilting-like) tendency is generally found here to be minimal except in a shallow layer at large box sizes.

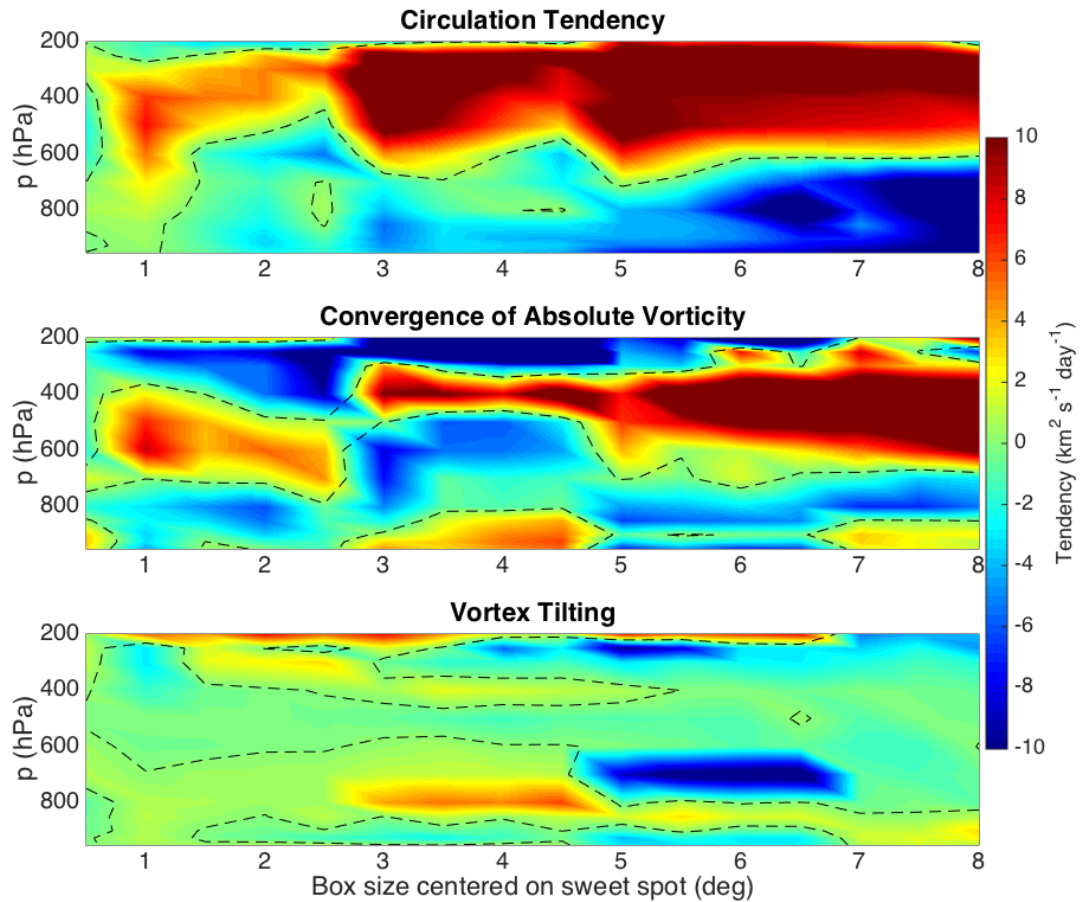


Figure 4.11: Time-height cross-sections of circulation (top), absolute vorticity convergence (middle), and vortex tilting (bottom) tendencies (shading) from 1800 UTC 11 September to 0000 UTC 12 September. The dashed line represents the zero contour level on each panel. This time interval is chosen to illustrate a low-level spin-down phase as indicated in Figures 4.6 and 4.8.

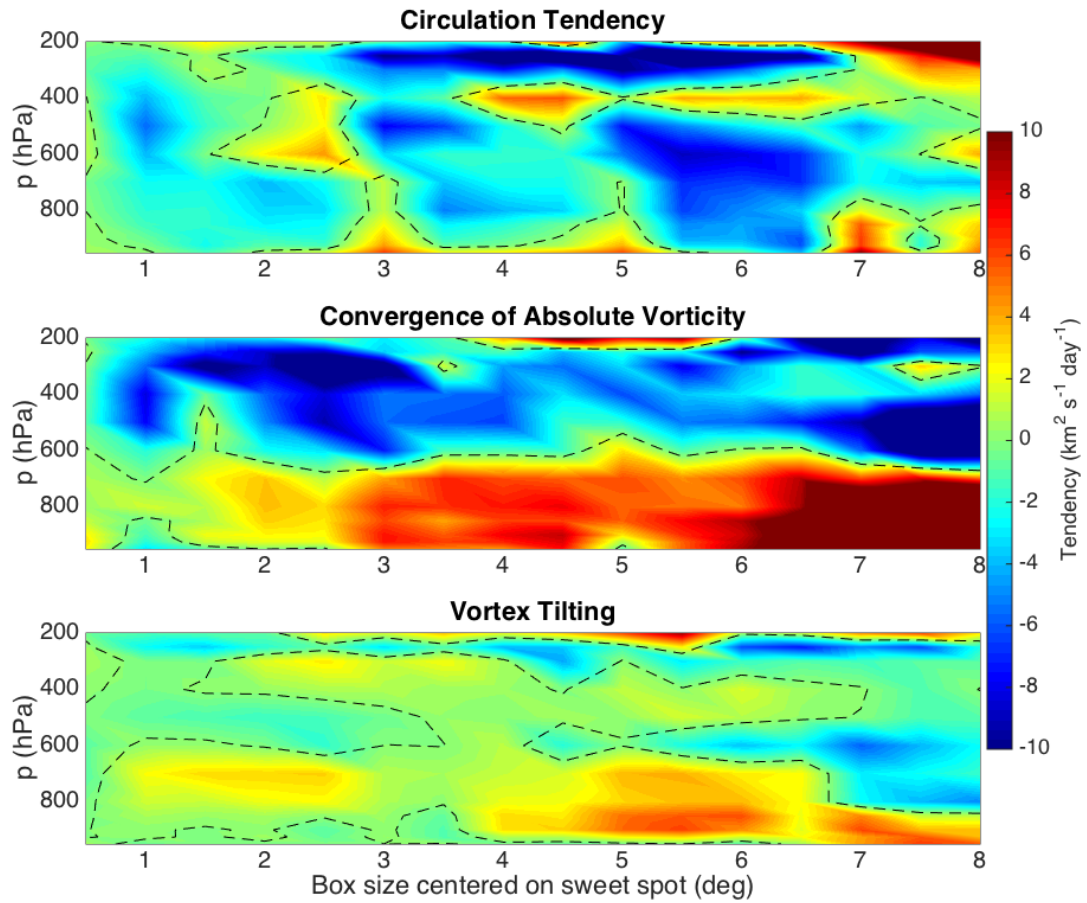


Figure 4.12: Time-height cross-sections of circulation (top), absolute vorticity convergence (middle), and vortex tilting (bottom) tendencies (shading) from 0000 UTC to 0600 UTC 12 September. The dashed line represents the zero contour level on each panel. This time interval is chosen to illustrate a low-level spin-up phase as indicated in Figures 4.6 and 4.8.

The pulsing of the circulation tendency continues until approximately 1800 UTC 14 September. At this time, the circulation and convergence of absolute vorticity tendencies are positive through a deep layer (Figure 4.13). This positive trend continues until Karl develops into a category 3 hurricane.

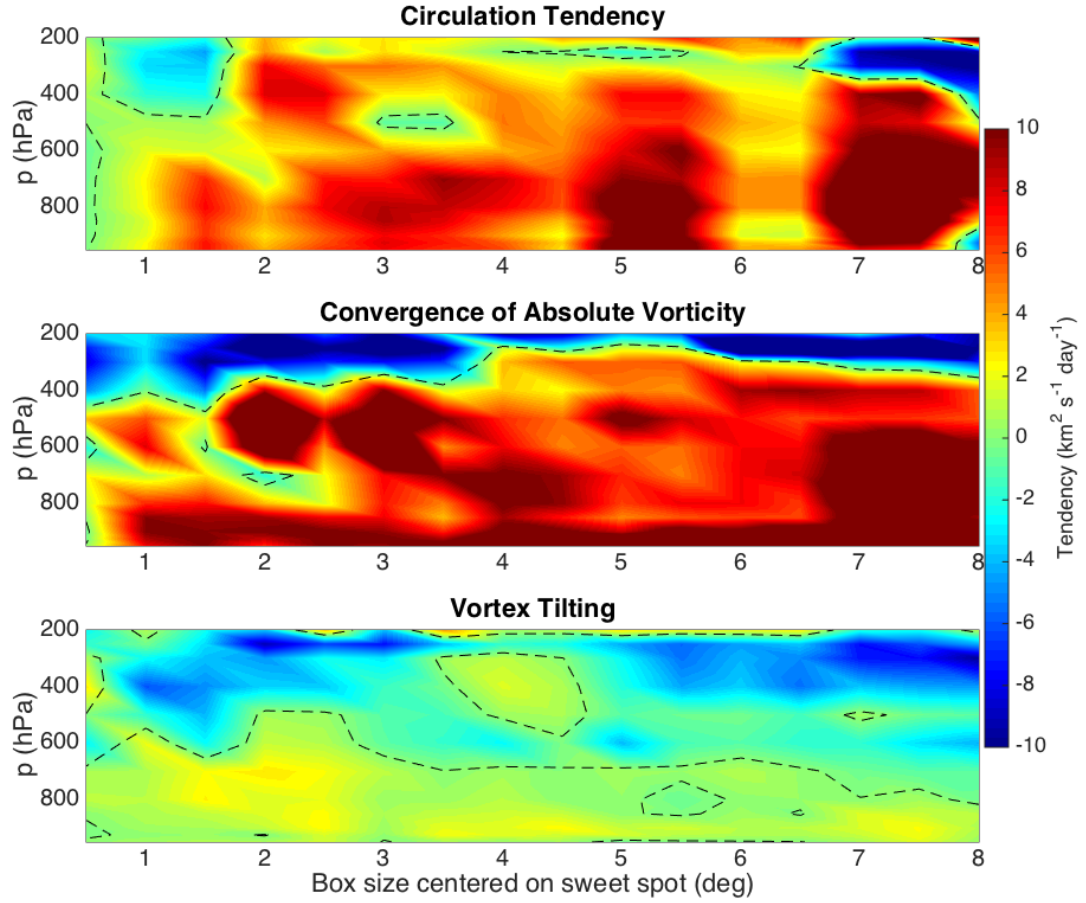


Figure 4.13: Time-height cross-sections of circulation (top), absolute vorticity convergence (middle), and vortex tilting (bottom) tendencies (shading) from 1200 UTC to 1800 UTC 14 September. The dashed line represents the zero contour level on each panel. NHC designated Karl a tropical storm at 2100 UTC 14 September.

At the time of the PREDICT mission, the science director provided two hypotheses for the pulsing nature of the relative vorticity and circulation tendency (Montgomery 2010b): (1) the diurnal cycle for convective activity or (2) a boundary layer recovery time-scale related to convective activity, itself. The second hypothesis assumes that each convective maximum is followed by a period of convective and mesoscale downdrafts. These downdrafts tend to flood the boundary layer with low  $\theta_e$  air. A period of boundary layer recovery is needed to increase  $\theta_e$  in the boundary layer back to pre-low  $\theta_e$  anomaly levels.

In the absence of such convective updraughts and downdraughts during this recovery period, Montgomery (2010b) suggests that a simple slab boundary layer model can be used to estimate the boundary layer recovery time-scale as:

$$T_r = \frac{h}{C_K v}, \quad (4.4)$$

where  $T_r$  is the recovery time,  $h$  is the depth of the boundary layer,  $C_K$  is the enthalpy exchange coefficient, and  $v$  is the near-surface wind speed. Using values of  $C_K = 1.2 \times 10^{-3}$  (Bell 2010),  $h = 0.5$  km, and  $v = 8 \text{ ms}^{-1}$ , one obtains  $T_r \approx 15$  h. Although this is an oversimplified model, Montgomery (2010b) finds this recovery time-scale is comparable to the period of observed convective activity and pulses in the relative vorticity and circulation. Montgomery (2010b) concludes that the periodic nature of the deep convective activity is result a of both the diurnal cycle in the Caribbean, as well as the boundary layer recovery time-scale.

### 4.3 Karl's Spin-Up

The circulation tendency results show an overall trend of Karl spinning-up from 10 to 17 September. A concomitant analysis is to study the evolution of the azimuthally-averaged absolute angular momentum surfaces and azimuthally averaged tangential velocity. The absolute angular momentum per unit mass,  $M$  is defined as follows:

$$M = rv + \frac{1}{2}fr^2, \quad (4.5)$$

where  $r$  is the radial distance to the sweet spot,  $v$  is the azimuthally averaged tangential velocity, and  $f$  is the Coriolis parameter at the sweet spot. In the absence of any torques (e.g., from eddy forcing, friction, or other subgrid-scale forcing), the absolute angular momentum is materially conserved (i.e.,  $DM/Dt = 0$ ). Equation (4.5) can also be re-written in terms of the azimuthally averaged tangential velocity as:

$$v = \frac{M}{r} - \frac{1}{2}fr. \quad (4.6)$$

When  $M$  is materially conserved,  $v$  is directly related to the radial distance,  $r$ , of the  $M$  surface from the sweet spot. As an air parcel gets closer to the sweet spot, the azimuthally

averaged tangential velocity must also increase. Therefore, a necessary condition for tropical cyclone spin-up, in an inviscid and axisymmetric framework, is radial inflow toward the sweet spot (Montgomery and Smith 2014).

Absolute angular momentum is approximately materially conserved above the frictional boundary layer. Deep convection near the sweet spot induces inflow above the boundary layer. Montgomery and Smith (2014) found in a number of idealized numerical simulations that above the frictional boundary layer, although the inflow is weak, the inflow is persistent. This persistent inflow draws  $M$  surfaces inwards, thus increasing the tangential winds above the boundary layer (Figure 4.14a,b).

Within the frictional boundary layer,  $M$  is not materially conserved. Friction reduces the tangential velocity in this layer. While the tangential velocity is decreasing, the radial component of pressure gradient remains unchanged, and results in an inward directed agradient force. This agradient force generates a strong radial inflow (Figure 4.14c) in the vortex boundary layer. Because of the frictional effects and the strong radial inflow, the  $M$  surfaces will tend to have a vertical gradient near the surface (Montgomery and Smith 2014). Figure 4.14d provides a summary depiction of this spin-up process involving both the deep convection and surface friction.

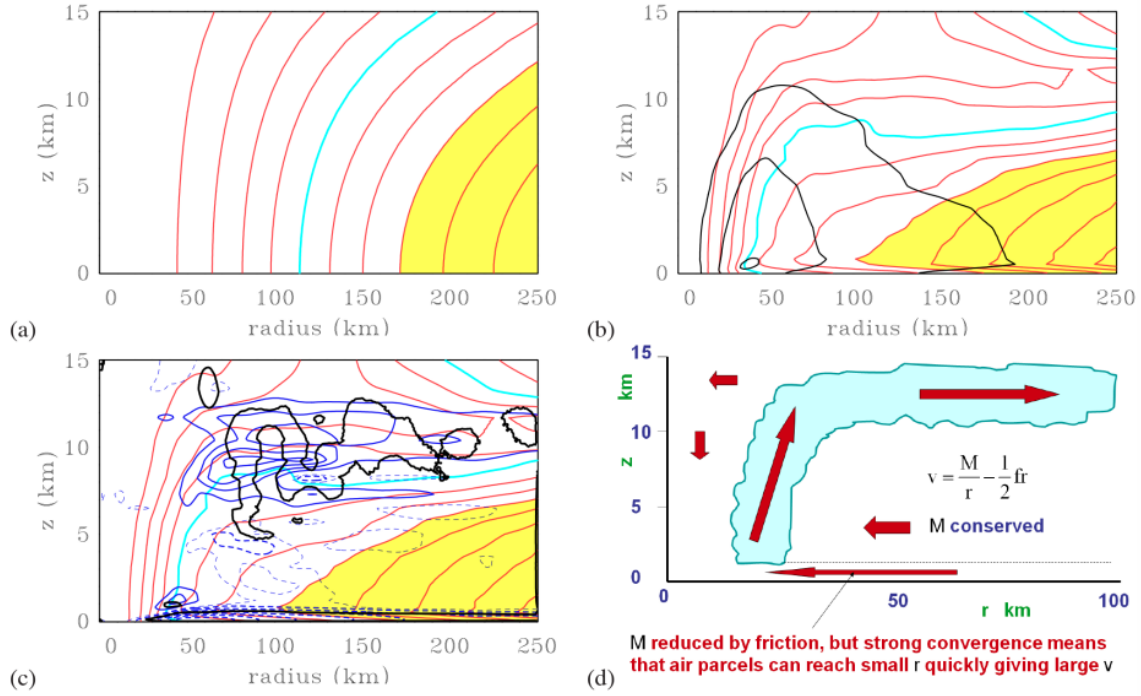


Figure 4.14: Absolute angular momentum surfaces (red and pink contours) at (a) initial time, and (b) 48 hours later from an idealized numerical experiment. The cyan contour indicates an  $M$  value of  $20 \times 10^5 \text{ m}^2 \text{ s}^{-1}$ , and the yellow region indicates values greater than  $32 \times 10^5 \text{ m}^2 \text{ s}^{-1}$ . Black contours in (b) are tangential velocity, and blue contours in (c) are radial velocities at 48 hours. The black contour in (c) delineates regions where conditions are met for axisymmetric instability (Montgomery and Smith 2014). (d) Depiction of the spin-up process (from Montgomery and Smith 2014).

To study the evolution of  $M$  surfaces (calculated as  $M = \Gamma_a / 2\pi$ ) for Karl, vertical profiles of  $M$  and  $v$  were made at each 6-hour timestep from 0000 UTC 10 September to 0000 UTC 17 September. These calculations assumed a constant  $f$  at each time interval and corresponded with the latitude of the tracking level sweet spot. The general trend shows the  $M$  surfaces moving inward throughout Karl's development (Figure 4.16). Initially, the radial inflow of air draws  $M$  surfaces in faster at larger radii. By 1800 UTC 13 September, the  $M$  surfaces are vertically uniform through a layer between 400 to 950 hPa. After 1800 UTC 13 September, the contours are continually drawn in through a deep layer. Within the frictional boundary layer however, the combination of friction and strong radial inflow creates the vertical gradient in the  $M$  surfaces calculated from the ECMWF analysis data. This

spin-up process is consistent with the intensification paradigm described in Montgomery and Smith (2014) and summarized conceptually in Figure 4.14d.

In a study of the structural evolution of Karl using the PREDICT data, Davis and Ahijevych (2012) observed a misalignment between the midlevel and low-level circulation centers (Figure 4.15). By 14 September, the circulation centers become aligned and further enhance a favorable formation environment as described in DMW09. With a favorable environment and pouch, pre-Karl transitioned into tropical storm Karl by 2100 UTC 14 September.

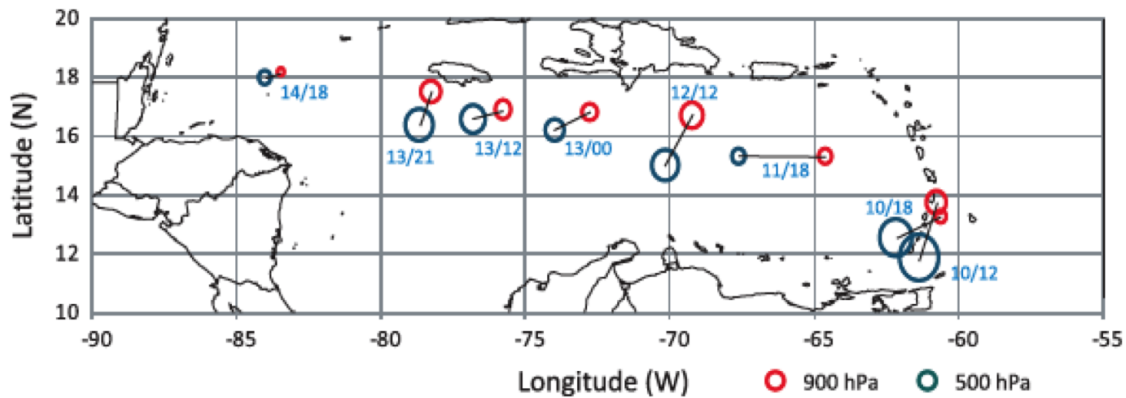


Figure 4.15: Pre-Karl circulation centers at 500 hPa (blue) and 900 hPa (red). The date and time of the analysis is indicated by the blue labels. The size of the circle is related to the spatial extent of the circulation (from Davis and Ahijevych 2012).

Combining the ideas of the inward-moving  $M$  surfaces and the approximate material conservation of  $M$ , Equation (4.6) shows that the tangential winds intensify. This amplification is, in fact, observed for Karl (Figure 4.16). Early in Karl's development, the maximum tangential wind is  $\sim 11 \text{ m s}^{-1}$  in a layer between 700 and 950 hPa. As the system develops, the tangential wind increases at all radii through a uniform, deep layer from 400 to 950 hPa. In general, the evolution of  $M$  surfaces and azimuthally averaged tangential wind implies that Karl underwent a low-level spin-up. This azimuthally-averaged perspective of Karl's development is similar to the findings of Lussier III et al. (2014) for Typhoon Nuri, and consistent with the intensification paradigm presented by Montgomery and Smith (2014).



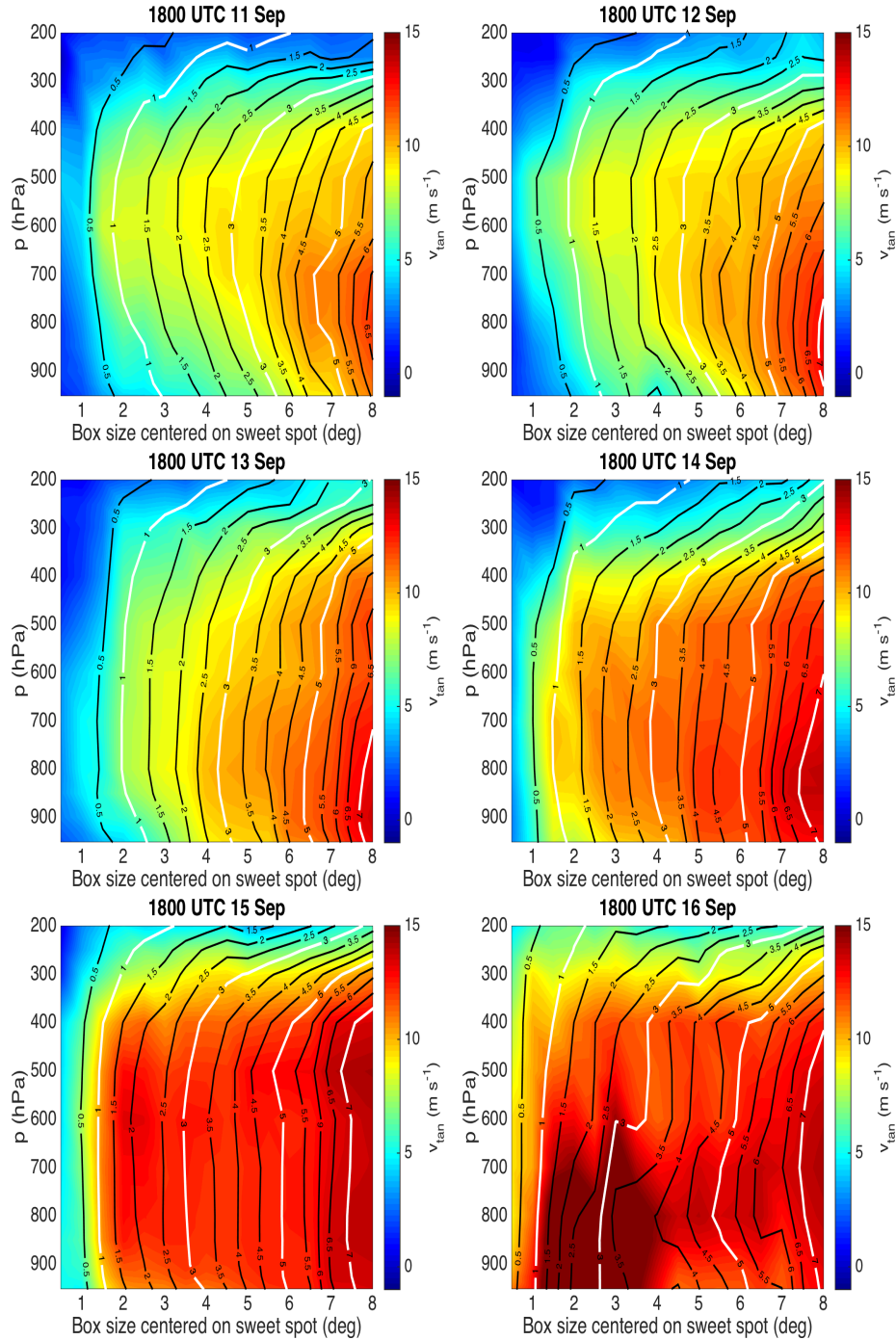


Figure 4.16: Evolution of average tangential velocity (shading) and angular momentum surfaces (contours) from 1800 UTC 11 September to 1800 UTC 16 September in 24 hour intervals as examples. The ordinate is pressure from 200 to 950 hPa and the abscissa is the size of a box centered on the sweet spot. Contours are shown for  $0.5 \times 10^6 \text{ m}^2 \text{ s}^{-1}$  intervals with the  $1, 3, 5,$  and  $7 \times 10^6 \text{ m}^2$  contours highlighted in white.

THIS PAGE INTENTIONALLY LEFT BLANK

---

## CHAPTER 5:

### Conclusions

---

The marsupial paradigm for tropical cyclogenesis hypothesizes that convective activity is favored within the protective region of a robust pouch (DMW09). Barring unfavorable circumstances like dry air intrusion or persistent vertical misalignment of the pouch, the theory hypothesizes that a developing system will exhibit a progressive moistening of the pouch by convection. Furthermore, vortical convective activity and convergence of vorticity near the sweet spot will amplify and aggregate vorticity in the pouch. Amplification and aggregation of vorticity will lead to the genesis of a tropical cyclone.

In this thesis, evidence is presented to suggest that both the non-developing case of ex-Gaston and developing case of Hurricane Karl support the marsupial paradigm for tropical cyclogenesis. Using the ECMWF analysis data, this thesis demonstrates that ex-Gaston did not have a robust pouch and was open to the intrusion of environmental air at the mid to upper levels on all days of the aircraft observations of this disturbance during PREDICT. Lagrangian trajectory and manifold calculations using ECMWF analyses show that dry air did indeed penetrate the pouch. These findings support the hypothesis that entrained, dry air near 600 hPa inhibited convective updraughts and vertical mass flux, which in turn leads to a reduction in vorticity and a compromised pouch at these middle levels. A compromised pouch allows further intrusion of dry air and inhibits subsequent vorticity amplification, as articulated in the work of Smith and Montgomery (2012). The findings presented herein support the original hypothesis that ex-Gaston's degraded pouch further led to the non-redevelopment of the system by limiting the amplification of vorticity and not providing a protected environment for sufficient vorticity aggregation, consistent with the marsupial paradigm of tropical cyclogenesis described by DMW09.

Unlike ex-Gaston, pre-Karl was embedded within a moist environment and developed into a tropical storm. Although Karl was not an African easterly wave (like ex-Gaston), a wave interaction with a mesoscale disturbance within the ITCZ led to the formation of a pouch (RM12). Despite forming in a favorable environment (warm SST, moist air, and low vertical shear), Karl had events of punctuated convection that resulted in both negative and

positive tendencies in the circulation throughout its development until its eventual genesis on 14 September. Davis and Ahijevych (2012) described the initial, vertical misalignment of Karl's pouch that helped to impede Karl's development. As this current study shows, by 1800 UTC 14 September (coincident with the vertical alignment of the pouch), convection within Karl's pouch was able to amplify relative vorticity; leading to a positive circulation tendency, an inward flux of angular momentum surfaces, and enhanced tangential wind. Karl's development is consistent with the three hypotheses of tropical cyclogenesis posited by DMW09 and summarized in Chapter 1 of this thesis, as well as with the intensification model described by Montgomery and Smith (2014).

---

## List of References

---

- Bechtold, P., M. Kohler, T. Jung, F. Doblas-Reyes, M. Leutbecher, M. J. Rodwell, F. Vitart, and G. Balsamo, 2008: Advances in simulating atmospheric variability with the ecmwf model: From synoptic to decadal time-scales. *Quart. J. Roy. Meteor. Soc.*, **134** (634), 1337–1352.
- Bechtold, P., N. Semane, P. Lopez, J.-P. Chaboureau, A. Beljaars, and N. Bormann, 2014: Representing equilibrium and nonequilibrium convection in large-scale models. *J. Atmos. Sci.*, **71** (2), 734–753.
- Bell, M. M., 2010: Air-sea enthalpy and momentum exchange at major hurricane wind speeds. Ph.D. thesis, Naval Postgraduate School, 155 pp.
- Bolton, D., 1980: The computation of equivalent potential temperature. *Mon. Wea. Rev.*, **108**, 1046–1053, doi:0027-0644/80/071046-0806.00.
- Boothe, M., 2015a: *POUCH TRACKING*. Accessed 31 August 2015. [Available online at <http://www.met.nps.edu/mtmontgo/storms2015-atlantic.html>].
- Davis, C., 2010a: Predict science director summary for 0900 UTC 09/11, <http://catalog.eol.ucar.edu/cgi-bin/predict/report/index>.
- Davis, C., 2010b: Predict science director summary for 10:10 UTC 09/13, <http://catalog.eol.ucar.edu/cgi-bin/predict/report/index>.
- Davis, C., and D. Ahijevych, 2012: Mesoscale structural evolution of three tropical weather systems observed during PREDICT. *J. Atmos. Sci.*, **69**, 1284–1305, doi:10.1175/JAS-D-11-0225.1.
- Dunkerton, T. J., M. T. Montgomery, and Z. Wang, 2009: Tropical cyclogenesis in a tropical wave critical layer: easterly waves. *Atmos. Chem. Phys. Disc.*, **8**, 11 149–11 292, doi:10.5194/acpd-8-11149-2008.
- Gjorgjievska, S., and D. J. Raymond, 2014: Interaction between dynamics and thermodynamics during tropical cyclogenesis. *Atmos. Chem. Phys.*, **14**, 3065–3082, doi:10.5194/acp-14-3065-2014.
- Haynes, P. H., and M. E. McIntyre, 1987: On the evolution of vorticity and potential vorticity in the presence of diabatic heating and frictional or other forces. *J. Atmos. Sci.*, **44** (5), 828–841, doi:10.1175/1520-0469(1987)044<0828:OTEOVA>2.0.CO;2.

- Hirose, M., R. Oki, S. Shimizu, M. Kachi, and T. Higashiuwatoko, 2008: Finescale diurnal rainfall statistics refined from eight years of trmm pr data. *J. Appl. Meteor. Climatol.*, **47** (2), 544–561.
- Ide, K., D. Small, and S. Wiggins, 2002: Distinguished hyperbolic trajectories in time-dependent fluid flows: analytical and computational approach for velocity fields defined as data sets. *Nonlinear Proc. Geoph.*, **9** (3/4), 237–263, doi:10.5194/npg-9-237-2002.
- James, R. P., and P. M. Markowski, 2010: A numerical investigation of the effects of dry air aloft on deep convection. *Mon. Wea. Rev.*, **138** (1), 140–161, doi:10.1175/2009MWR3018.1.
- Kilroy, G., and R. K. Smith, 2012: A numerical study of rotating convection during tropical cyclogenesis. *Quart. J. Roy. Meteor. Soc.*, **139** (674), 1255–1269, doi:10.1002/qj.2022.
- Köhler, M., M. Ahlgrim, and A. Beljaars, 2011: Unified treatment of dry convective and stratocumulus-topped boundary layers in the ecmwf model. *Quart. J. Roy. Meteor. Soc.*, **137** (654), 43–57.
- Komaromi, W. A., 2013: An investigation of composite dropsonde profiles for developing and nondeveloping tropical waves during the 2010 predict field campaign. *J. Atmos. Sci.*, **70** (2), 542–558.
- Lussier III, L., 2010: A multi-scale analysis of the tropical cyclogenesis within the critical layer of tropical easterly waves in the atlantic and western north pacific sectors. Ph.D. thesis, Naval Postgraduate School, 247 pp.
- Lussier III, L., M. Montgomery, and M. Bell, 2014: The genesis of Typhoon Nuri as observed during the Tropical Cyclone Structure 2008 (TCS-08) field experiment - Part 3: Dynamics of low-level spin-up during the genesis. *Atmos. Chem. Phys.*, **14**, 8795–8812, doi:10.5194/acp-14-8795-2014.
- Lussier III, L., B. Rutherford, M. Montgomery, and M. Boothe, 2015: Examining the roles of the easterly wave critical layer and vorticity accretion during the tropical cyclogenesis of Hurricane Sandy. *Mon. Wea. Rev.*, **143**, 1703–1722, doi:10.1175/MWR-D-14-00001.1.
- Mlawer, E. J., S. J. Taubman, P. D. Brown, M. J. Iacono, and S. A. Clough, 1997: Radiative transfer for inhomogeneous atmospheres: Rrtm, a validated correlated-k model for the longwave. *JGR: Atmospheres (1984–2012)*, **102** (D14), 16 663–16 682.
- Montgomery, M. T., 2010a: *NSF PREDICT (2010) HYPOTHESES*. Accessed 31 August 2015. [Available online at <http://www.met.nps.edu/mtmontgo/marsupial.html>].

- Montgomery, M. T., L. Lussier, R. Moore, and Z. Wang, 2010a: The genesis of Typhoon Nuri as observed during the Tropical Cyclone Structure 2008 (TCS-08) field experiment - Part 1: The role of the easterly wave critical layer. *Atmos. Chem. Phys.*, **10**, 9879–9900, doi:10.5194/acp-10-9879-2010.
- Montgomery, M. T., and R. K. Smith, 2014: Paradigms for tropical cyclone intensification. *Aust. Meteor. Oceanogr. J.*, **64**, 1–30.
- Montgomery, M. T., Z. Wang, and T. Dunkerton, 2010b: Coarse, intermediate and high resolution numerical simulations of the transition of a tropical wave critical layer to a tropical storm. *Atmos. Chem. Phys.*, **10**, 10 803–10 827, doi:10.5194/acp-10-10803-2010.
- Montgomery, M. T., and Coauthors, 2012: The pre-depression investigation of cloud-systems in the tropics (PREDICT) experiment: Scientific basis, new analysis tools, and some first results. *Bull. Amer. Meteor. Soc.*, **93** (2), 153–172, doi:10.1175/BAMS-D-11-00046.1.
- Montgomery, T., Michael, 2010b: Predict science director summary for 14:35 UTC 09/14, <http://catalog.eol.ucar.edu/cgi-bin/predict/report/index>.
- Morcrette, J., H. Barker, J. Cole, M. Iacono, and R. Pincus, 2008: Impact of a new radiation package, mcrad, in the ecmwf integrated forecasting system. *Mon. Wea. Rev.*, **136** (12), 4773–4798.
- Nicholls, M. E., and M. T. Montgomery, 2013: An examination of two pathways to tropical cyclogenesis occurring in idealized simulations with a cloud-resolving numerical model. *Atmos. Chem. Phys.*, **13** (12), 5999–6022, doi:10.5194/acp-13-5999-2013.
- Raymond, D. J., S. Gjorgjievska, S. Sessions, and Ž. Fuchs, 2014: Tropical cyclogenesis and mid-level vorticity. *Aust. Met. Ocean. Soc. J. J. J. J.*, 11–25.
- Raymond, D. J., and C. Lopez-Carrillo, 2011: The vorticity budget of developing typhoon Nuri (2008). *Atmos. Chem. Phys.*, **11** (1), 147–163, doi:10.5194/acp-11-147-2011.
- Raymond, D. J., and S. L. Sessions, 2007: Evolution of convection during tropical cyclogenesis. *Geophys. Res. Lett.*, **34** (6).
- Riemer, M., and M. T. Montgomery, 2011: Simple kinematic models for the environmental interaction of tropical cyclones in vertical wind shear. *Atmos. Chem. Phys.*, **11** (17), 9395–9414, doi:10.5194/acp-11-9395-2011.
- Rutherford, B., and M. T. Montgomery, 2012: A Lagrangian analysis of a developing and non-developing disturbance observed during the PREDICT experiment. *Atmos. Chem. Phys.*, **12**, 11 355–11 381, doi:10.5194/acp-12-11355-2012.

- Samelson, R. M., and S. Wiggins, 2006: *Lagrangian transport in geophysical jets and waves: the dynamical systems approach*, Vol. 31. Springer Science & Business Media, Berlin.
- Sauer, W., 2014: Thermodynamic and kinematic flow characteristics of some developing and non-developing disturbances in PREDICT. M.S. thesis, Dept. of Meteorology, Naval Postgraduate School, 142 pp.
- Smith, R. K., and M. T. Montgomery, 2012: Observations of the convective environment in developing and non-developing tropical disturbances. *Quart. J. Roy. Meteor. Soc.*, **138**, 1721–1739, doi:10.1002/qj.1910.
- Sorooshian, S., X. Gao, K. Hsu, R. Maddox, Y. Hong, H. Gupta, and B. Imam, 2002: Diurnal variability of tropical rainfall retrieved from combined goes and trmm satellite information. *J. Climate*, **15** (9), 983–1001.
- Tiedtke, M., 1989: A comprehensive mass flux scheme for cumulus parameterization in large-scale models. *Mon. Wea. Rev.*, **117** (8), 1779–1800.
- Wang, Z., 2012: Thermodynamic aspects of tropical cyclone formation. *J. Atmos. Sci.*, **69** (8), 2433–2451.
- Wang, Z., M. T. Montgomery, and T. J. Dunkerton, 2010a: Genesis of Pre-Hurricane Felix (2007). Part I: The role of the easterly wave critical layer. *J. Atmos. Sci.*, **67** (6), 1711–1729, doi:10.1175/2009JAS3420.1.
- Wang, Z., M. T. Montgomery, and T. J. Dunkerton, 2010b: Genesis of Pre-Hurricane Felix (2007). Part II: Warm Core Formation, Precipitation Evolution, and Predictability. *J. Atmos. Sci.*, **67** (6), 1730–1744, doi:10.1175/2010JAS3435.1.
- Wang, Z., M. T. Montgomery, and T. J. Dunkerton, 2009: A dynamically-based method for forecasting tropical cyclogenesis location in the atlantic sector using global model products. *Geophys. Res. Lett.*, **36** (3).



---

## Initial Distribution List

---

1. Defense Technical Information Center  
Ft. Belvoir, Virginia
2. Dudley Knox Library  
Naval Postgraduate School  
Monterey, California